UNIVERSITÀ DEGLI STUDI DI PADOVA

Dipartimento di Fisica e Astronomia "Galileo Galilei"

Master Degree in Physics

Final Dissertation

Kinematic Sunyaev-Zel'dovich effect: non-linear modelling of the velocity field for cosmological and astrophysical applications.

Thesis supervisor:

Prof. Sabino Matarrese

Thesis co-supervisor:

Dr. Carlo Schimd

Candidate:

Amalia Basiricò

Academic Year 2023/2024

Contents

Introduction

Modern cosmology is built on three main observational facts which support the Big Bang theory: expansion of the universe, the abundance of elements lighter than ^{8}Be and the isotropy of the Cosmic Microwave Background (CMB) radiation.

The CMB is the cooled remnant of the first light emitted after the electron-proton recombination and probing the photon decoupling from the primeval plasma, occurring at redshift $z \simeq 1100$, before any stars or galaxies formed in the Universe. It has a nearly perfect black body spectrum with temperature $T_{\rm CMB} = 2.72548(57)$ K (Fixsen 2009), with tiny fluctuations of order 10^{-5} characteristic of an almost Gaussian random field (citazioni ultimi lavori Planck). The so-called *primary anisotropies* originated at the time of recombination, while *secondary anisotropies* anisotropies are imprinted on the CMB at a later time, as the photons propagate through the Universe and interact with cosmic structure that formed since. Secondary anisotropies are perturbations of the genuine cosmological CMB signal, as they change the temperature information that they carry, however, they also carry a wealth of information about the cosmic distribution of matter.

The Sunyaev-Zel'dovich (SZ) effects (Sunyaev & Zel'dovich 1970) are an important source of secondary anisotropy, causing a change in the apparent brightness of the CMB towards clusters of galaxies or any other reservoir of hot ionised gas. Thermal and kinematic effects, are both originated by the inverse Compton scattering of CMB photons by free electrons, which are particularly abundant in galaxy clusters and groups. The thermal contribution is due to the thermal motion of electrons in the ionised gas, while the kinematic effect results from the bulk proper motion of the gas reservoir, which does not include the Hubble drift.

In the gravitational instability picture perturbations of the background energy density distribution grow with time, inducing peculiar (local) motions that deviate from the Hubble flow. The motions of fundamental observers with respect to the cosmological rest frame define the so called peculiar velocity field. Peculiar velocities can be a useful cosmological probe, as they are sensitive to the matter distribution on large scales offering a test of the link between gravity and matter. Unfortunately, the direct measurement of peculiar velocities on cosmological scales is limited to the nearby universe, up to few hundreds of Mpc, requiring indirect reconstruction methods based on the observed matter distribution and requiring the assumption of a cosmological model (formerly/sometimes dubbed "distance cosmology") to transform observed angular positions and redshift into

comoving distances and ultimately 3D positions; this is therefore a folded non-linear problem. Techniques of velocity reconstruction fail especially at high redshifts and on small scales, where observations are limited to the brightest objects (completeness of catalogues) and still limited to partial portions of the full sky.

The kinematic Sunyaev-Zel'dovich (kSZ) effect, which is proportional to the bulk peculiar velocity of ionised gas reservoirs along an observer's line-of-sight. It does not depend on redshift offering a unique probe of the cosmic peculiar velocity field on intermediate and large scales. The goal of this study is to test how well a non-linear peculiar velocity model perform when compared to the linear first-order Eulerian perturbation theory, routinely adopted to analyse kSZ catalogues.

In modern understanding of galaxy formation, every galaxy forms within a dark matter halo. The formation and growth of galaxies over time is connected to the growth of the haloes in which they form, with secondary (though important) effect of the environment via tidal gravitational interactions and feedback mechanisms induced by stellar and AGN activity.

The advent of large galaxy surveys and high-resolution cosmological simulations is providing new hints into the relationship between galaxies and haloes and its evolution. In this study we explore the kSZ using a specific suite of cosmological hydrodynamical simulations that solve the dynamics of matter fields on scales large enough to be used for a kSZ study and implement feedback mechanisms able to reproduce the observations on galaxy cluster scales (Hirschmann et al. 2014; Dolag et al. 2015).

Chapter 1

The Sunyaev-Zel'dovich effect

1 Intensity spectrum distortion

The Sunyaev-Zel'dovich effect (Sunyaev, Zeldovich, 1969; 1970; 1972) is the distortion of the Cosmic Microwave Background (CMB) radiation caused by the inverse Compton scattering of CMB photons off energetic electrons in clusters of galaxies, or any other reservoir of hot ionised gas. The effect causes a change in the apparent brightness of the CMB, i.e. a distortion of the CMB black-body spectrum in the direction of hot ionized gas reservoirs, and is not affected by dimming at high redshift since it is nearly z independent, therefore providing a robust cosmological probe. It also offers a very powerful tool for investigating the properties of gas in galaxy clusters, its distribution and kinematics at a wide range of redshifts.

1.1 Overview

The **tSZ effect** follows the characteristic frequency dependence given by

$$f(x, T_{\rm e}) = \frac{x^4 e^x}{\left(e^x - 1\right)^2} \left(x \coth\left(\frac{x}{2}\right) - 4 \right) \left(1 + \delta_{\rm tSZ}(x, T_{\rm e})\right), \tag{1.1}$$

where $x = h\nu / k_{\rm B} T_{\rm CMB}$ is the dimensionless frequency, with h Planck's constant, ν the frequency in the observer's frame, $k_{\rm B}$ Boltzmann's constant, and $T_{\rm CMB} = 2.72548(57)$ K the CMB temperature. The term $\delta_{\rm tSZ}$ accounts for relativistic corrections, which depend on x and the electron temperature T_e, but it can be reasonably approximated by a constant value and so neglected.

The spectral dependence of the **kSZ effect** is given by

$$g(x, T_{\rm e}, v_{\parallel}) = \frac{x^4 e^x}{\left(e^x - 1\right)^2} \left(1 + \delta_{\rm kSZ}(x, T_{\rm e}, v_{\parallel})\right), \tag{1.2}$$

where $v_{\parallel}$ is the component of the peculiar velocity $v_{\rm p}$ along the line-of-sight (positive for a cluster receding from the observer) and $\delta_{\rm kSZ}$ are the relativistic corrections that

depend on x, T_e, and $v_\parallel$. The velocity dependence on these corrections is negligible because $v_\parallel$ is always much smaller than the speed of light. For non-relativistic plasma $g(x, T_\mathrm{e}, v_\parallel)$ simplifies to

$$g(x) = \frac{x^4 e^x}{\left(e^x - 1\right)^2}\,, \tag{1.3}$$

thus in the non-relativistic regime the kSZ spectrum has the same shape of that of primary CMB anisotropies.

The observed change of specific intensity expressed as a function of ν, ΔI_ν, with scaling $I_0 = (2h/c^2)(k_\mathrm{B}T_\mathrm{CMB}/h)^3$, is given by

$$\frac{\Delta I_\nu}{I_0} = f(\nu, T_\mathrm{e})\, y_\mathrm{tSZ} + g(\nu, T_\mathrm{e}, v_\parallel)\, y_\mathrm{kSZ}\,, \tag{1.4}$$

where the amplitudes y (also called Comptonisation parameters) of the tSZ and the kSZ are respectively given by

$$\begin{aligned} y_\mathrm{tSZ} &= \frac{\sigma_\mathrm{T}}{m_e c^2}\int P_\mathrm{e}\mathrm{d}l \equiv \frac{k_\mathrm{B}T_\mathrm{e}}{m_\mathrm{e}c^2}\tau_\mathrm{e}\,, \\ y_\mathrm{kSZ} &= -\sigma_\mathrm{T}\int \frac{v_\parallel}{c} n_\mathrm{e}\mathrm{d}l \equiv -\frac{v_\parallel}{c}\tau_\mathrm{e}\,, \end{aligned} \tag{1.5}$$

in which the integral is computed over the gas reservoir width along the line-of-sight parametrised by the physical distance l, P_e, m_e and n_e are respectively the pressure, mass, and number density of the free electrons and $\tau_\mathrm{e} = \int \mathrm{d}l\, \sigma_\mathrm{T} n_\mathrm{e}$ is the optical depth fixed by the Thomson cross-section σ_T. The detailed derivation of the two effects will be carried out in the forthcoming paragraphs. The shape of the spectral deformations due to SZ signals are shown in Figure 1.1, alongside the deformation due to relativistic corrections which will also be discussed more in depth in Section 1.5 Chapter 1.

Typical clusters contain electrons with $k_\mathrm{B}T_\mathrm{e} \approx 5-10$ keV, or $k_\mathrm{B}T_\mathrm{e}/m_\mathrm{e}c^2 \approx 0.01-0.02$ and their central optical depth can reach $\tau_0 \approx 10^{-2}$, such that for massive clusters (e.g. $M_{200\mathrm{c}} \approx 10^{15} h^{-1} M_\odot$) $y_\mathrm{tSZ} \approx 10^{-4}$. The expected typical peculiar motions of clusters in the standard cosmological model are $\beta_\mathrm{p} = v_\mathrm{p}/c \lesssim 10^{-3}$, such that $y_\mathrm{kSZ} \lesssim 10^{-5}$. This is about one order of magnitude smaller than the typical tSZ y-parameter. For this reason the kSZ anisotropy is more challenging to observe, being subdominant to the tSZ unless the bulk velocity reaches a few tenths of a percent of the speed of light. Thus observations of the kSZ signal are best made at frequencies near the null of the tSZ effect (see Figure 1.1), i.e. for $x_0 \sim 3.83$ or $\nu_0 \sim$218 GHz. In addition, the spectral dependence of the kSZ is the same as that of primary CMB anisotropies, so that they can only be distinguished and separated from each other looking at the difference in spatial distribution of the two signals. SZ effects are indeed localised as they appear towards cluster of galaxies, furthermore the amplitude of their signals is likely related to other observable properties of clusters. Primordial anisotropies of the CMB are instead not localised, i.e. they are not associated with any structure and randomly distributed over the entire sky.

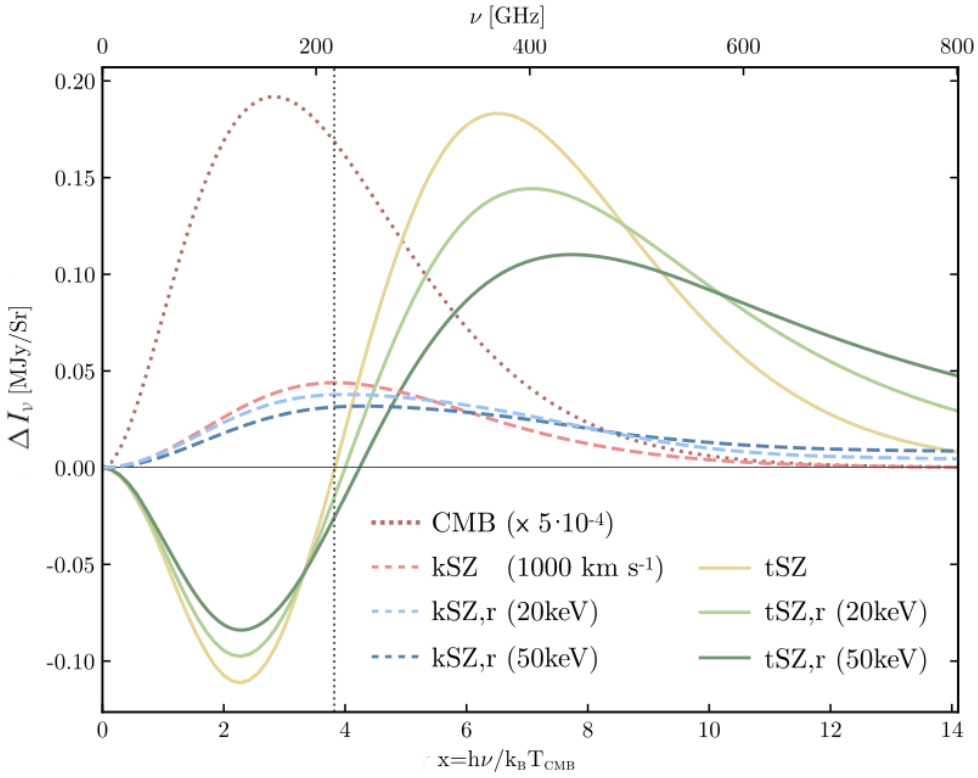

Figure 1.1: Thermal (solid) and kinematic (dashed) SZ spectra, also showing relativistic corrections for $k_{\rm B}T_e = 20$ keV and $k_{\rm B}T_e = 50$ (labelled *kSZ,r* and *tSZ,r*), assuming an optical depth $\tau_{\rm e} = 10^{-2}$ characteristic for clusters of mass $M_{200c} \approx 10^{15}$, an overall Compton parameter $y = 10^{-4}$, and $v_p = 1000$ km s^{-1}. For reference thermal spectrum for the CMB intensity scaled by a factor of 5×10^{-4} is shown by the dotted-dark-red curve (Mroczkowski et al. 2019).

1.2 Inverse Compton scattering

The theoretical foundation of the SZ effect is the inverse-Compton scattering of the photons of the CMB to higher energy photons by free electrons in ionised gas reservoirs. A single photon-electron scattering causes a photon having an initial energy ε in the rest frame of the scattering electron, to emerge after the scattering with a final energy ε' given by

$$\varepsilon' = \frac{\varepsilon}{1 + (\varepsilon/m_{\rm e}c^2)(1 - \cos\phi_{12})}\,, \tag{1.6}$$

where ϕ_{12} is the angle by which the photon is deflected. The cross-section $\mathrm{d}\sigma/\mathrm{d}\Omega$ of the scattering of a photon with energies ϵ and ϵ', is in general described by Klein-Nishina formula

$$\frac{\mathrm{d}\sigma}{\mathrm{d}\Omega} = \frac{r_{\rm e}^2}{2}\left(\frac{\epsilon'}{\epsilon}\right)^2\left(\frac{\epsilon}{\epsilon'} + \frac{\epsilon'}{\epsilon} - \sin^2\phi_{12}\right)\,. \tag{1.7}$$

For the case of Compton scattering among non-relativistic or mildly relativistic electrons the scatter is almost elastic ($\varepsilon' \approx \varepsilon$) since $\varepsilon \ll m_\mathrm{e}c^2$ holds in the reference frame of the scattering electron. This limit is appropriate for describing scatterings occurring in clusters of galaxies that cause the tSZ effect. In this low-energy limit the Klein-Nishina formula (1.7), recalling $\sigma_\mathrm{T} = (8\pi/3)r_\mathrm{e}^2$, reduces to the classical Thomson cross-section expression

$$\frac{\mathrm{d}\sigma}{\mathrm{d}\Omega} = \frac{3\sigma_\mathrm{T}}{16\pi}(1+\cos^2\phi_{12})\,. \tag{1.8}$$

This approximation affects the calculation of the Comptonisation parameter y. For a thermal population of electrons giving rise to the tSZ effect the Thomson limit is valid, therefore σ_T appears in the definition (1.5) of y_tSZ.

The probability of a scattering having an incoming photon from the direction $\mu = \cos\theta$ with respect to the electron velocity $v = \beta c$ (with corresponding Lorentz factor γ in the scattering electron reference frame) is

$$p(\mu) = \frac{1}{2\gamma^4(1-\beta\mu)^3}\,. \tag{1.9}$$

The photon redistribution, that is the probability of a scatter to a direction $\mu' = \cos\theta'$, is

$$\phi(\mu'|\mu) = \frac{3}{8}\left[1+\mu^2\mu'^2+\frac{1}{2}(1-\mu^2)(1-\mu'^2)\right]\,. \tag{1.10}$$

The change in direction of the photon causes a frequency change from ν to ν' for the scattered photon. The logarithmic frequency shift is then defined as

$$s = \log\left(\frac{\nu'}{\nu}\right) = \log\left(\frac{1+\beta\mu'}{1-\beta\mu}\right)\,. \tag{1.11}$$

The probability that a single scattering of a photon from an electron with speed $v = \beta c$ causes a frequency shift s is

$$P(s|\beta) = \int \mathrm{d}\mu\, p(\mu)\phi(\mu'|\mu)\left(\frac{\mathrm{d}\mu'}{\mathrm{d}s}\right)\,. \tag{1.12}$$

Substituting equations (1.9) and (1.10) into (1.12), and obtaining $\mathrm{d}\mu'/\mathrm{d}s$ from equation (1.11), the probability can be rewritten as

$$P(s|\beta) = \frac{3}{16\gamma^4\beta}\int \frac{(1+\beta\mu')}{(1-\beta\mu)^3}\left[1+\mu^2\mu'^2+\frac{1}{2}(1-\mu^2)(1-\mu'^2)\right]\mathrm{d}\mu\,. \tag{1.13}$$

The overall distribution of photon frequency shift due to an electron population can be obtained by integrating $P(s|\beta)$ over the electron β distribution. Supposing that the latter is Maxwellian, one obtains

$$P_1(s) = \frac{\int \beta^2\gamma^5 e^{-\eta(\gamma-1)}P(s|\beta)\mathrm{d}\beta}{\int \beta^2\gamma^5 e^{-\eta(\gamma-1)}\mathrm{d}\beta}\,, \tag{1.14}$$

with $\eta = (m_\mathrm{e}c^2)/(k_\mathrm{B}T_\mathrm{e})$.

The single scattering frequency shift is then used to obtain the form of the scattered spectrum of the CMB

$$\frac{I(\nu)}{h\nu} = \int_0^\infty \mathrm{d}\nu_0 \, P_1(\nu,\nu_0)\frac{I_0(\nu_0)}{h\nu_0}\,, \tag{1.15}$$

where $I_0(\nu_0)$ is the incident radiation intensity, given by the usual Plank distribution for the CMB photons

$$I_0(\nu) = \frac{2h\nu^3}{c^2}\left(\mathrm{e}^{h\nu/k_\mathrm{B}T_\mathrm{CMB}} - 1\right)^{-1}, \tag{1.16}$$

$P_1(\nu,\nu_0)$ is the probability that a scattering occurs from frequency ν_0 to ν, and $I(\nu)/h\nu$ is the spectrum in terms of photon number. Since $P_1(\nu,\nu_0) = P_1(s)/\nu$, equation (1.15) can be rewritten in terms of $s = \ln(\nu/\nu_0)$ as

$$I(\nu) = \int_{-\infty}^{\infty} P_1(s) I_0(\nu_0)\,\mathrm{d}s\,. \tag{1.17}$$

The change in the radiation spectrum at frequency ν is then

$$\Delta I(\nu) \equiv I(\nu) - I_0(\nu) = \frac{2h}{c^2}\int_{-\infty}^{\infty} P_1(s)\left(\frac{\nu_0^3}{e^{h\nu_0/k_\mathrm{B}T_\mathrm{rad}}-1} - \frac{\nu^3}{e^{h\nu/k_\mathrm{B}T_\mathrm{rad}}-1}\right)\mathrm{d}s \tag{1.18}$$

In reality a photon entering the election distribution undergoes many scatterings, the resulting intensity change is then reduced by a factor τ_e, that is the electron distribution optical depth, so finally

$$\Delta I(\nu) = \frac{2h}{c^2}\,\tau_\mathrm{e}\int_{-\infty}^{\infty} P_1(s)\left(\frac{\nu_0^3}{e^{h\nu_0/k_\mathrm{B}T_\mathrm{rad}}-1} - \frac{\nu^3}{e^{h\nu/k_\mathrm{B}T_\mathrm{rad}}-1}\right)\mathrm{d}s\,. \tag{1.19}$$

One important result is already clear from this expression: the intensity change caused by the SZ effect does not depend on redshift but only on intrinsic properties of the scattering medium given by τ_e and $P_1(s)$, while the dependence on z is integrated out via the integral over s. $P_1(s)$ is given by equation (1.14), or alternatively and more often derived as solution of the Kompaneets equation; see next section.

1.3 Thermal Sunyaev-Zel'dovich (tSZ)

The tSZ effect is caused by the thermal motion of the electrons in a hot plasma, resulting in a characteristic spectral distortion to the CMB blackbody radiation. The derivation of expression (1.19) takes into account the relativistic kinematics and statistics of the scattering process, while for a typical thermal electron population the random velocities are still non-relativistic.

The photon occupation number distribution (or photon number density) n due to a non-relativistic diffusion process is accounted for by the Kompaneets (1956) equation

$$\frac{\partial}{\partial y}n(x,y) = \frac{1}{x^2}\frac{\partial}{\partial x}\left(x^4\frac{\partial}{\partial x}n(x,y)\right)\,, \tag{1.20}$$

where $x = h\nu/k_{\rm B}T_{\rm CMB}$ is the adimensional photon energy and y is the Comptonisation parameter of tSZ, defined in equation (1.5) and reported here for clarity

$$y = \int {\rm d}l\, n_{\rm e}\sigma_T \frac{k_{\rm B}T_{\rm e}}{m_{\rm e}c^2}\,. \tag{1.21}$$

It determines the amount of diffusion characterising the solution of the Kompaneets equation.

The formal solution of equation (1.20) is obtained by integrating over y, yielding

$$n(x,y) = \exp\left(\frac{y}{x^2}\frac{\partial}{\partial x}x^4\frac{\partial}{\partial x}\right) n(x,0)\,, \tag{1.22}$$

where $n(x,0)$ is the occupation number distribution in absence of diffusion, $y = 0$. Since the undistorted photon spectrum remains that of a black-body, one can set

$$n(x,0) = \frac{1}{e^x - 1}\,. \tag{1.23}$$

As long as $x^2 y < 1$, typical for small values of y and frequencies around GHz, the equation (1.22) admits a Taylor expansion, such that

$$\begin{aligned} n(x,y) &\approx n(x,0) + \frac{y}{x^2}\frac{\partial}{\partial x}\left(x^4\frac{\partial}{\partial x}n(x,0)\right) \\ &= \frac{1}{e^x-1} + \frac{y}{x^2}\frac{\partial}{\partial x}\left(x^4\frac{\partial}{\partial x}\frac{1}{e^x-1}\right) \\ &= \frac{1}{e^x-1} + \frac{yxe^x}{(e^x-1)^2}\left(x\coth\left(\frac{x}{2}\right) - 4\right), \end{aligned} \tag{1.24}$$

therefore the absolute variation of the number density reads

$$\Delta n(x,y) = \frac{yxe^x}{(e^x-1)^2}\left(x\coth\left(\frac{x}{2}\right) - 4\right), \tag{1.25}$$

which corresponds to a change of intensity

$$\Delta I(x) = x^3 \Delta n(x) I_0\,, \tag{1.26}$$

where $I_0 = 2h/c^2(k_{\rm B}T_{\rm CMB}/h)^3$ and y has been considered as a fixed parameter $y \equiv y_{\rm tSZ}$ (it has a fixed value for each cluster). Finally one obtains

$$\Delta I = y_{\rm tSZ} I_0 \frac{x^4 e^x}{(e^x-1)^2}\left(x\coth\left(\frac{x}{2}\right) - 4\right) \equiv y_{\rm tSZ} I_0 f(x)\,, \tag{1.27}$$

and

$$\Delta T_{\rm tSZ} = T_{\rm CMB}\frac{\Delta I}{x^2 I_0} = y_{\rm tSZ} T_{\rm CMB}\,\frac{x^2 e^x}{(e^x-1)^2}\left(x\coth\left(\frac{x}{2}\right) - 4\right). \tag{1.28}$$

Dealing with observations, it is useful to avail of $n(x, y)$ to compute the so-called effective blackbody temperature $T_y(x)$ defined as

$$\frac{T(x)_y}{T_{\rm CMB}} = \frac{x}{\ln\left(1 + n(x,y)^{-1}\right)} \,. \tag{1.29}$$

For $n(x, 0)$, which is the pure blackbody distribution, one gets $T(x)_{y=0}/T_{\rm CMB} = 1$, hence the relation (1.29) is a useful way of characterising departures from the blackbody spectrum. For the approximate $n(x, y)$ given by equation (1.24),

$$\frac{T(x)_y}{T_{\rm CMB}} \approx 1 + y\left(x\coth\left(\frac{x}{2}\right) - 4\right) \,. \tag{1.30}$$

In the Rayleigh-Jeans limit $x \to 0$

$$\frac{T_y}{T_{\rm CMB}} \to 1 - 2y \,, \tag{1.31}$$

so that, for $y = y_{\rm tSZ}$ fixed at the value of a specific source (e.g. galaxy cluster),

$$\frac{\Delta T_{\rm tSZ}}{T_{\rm CMB}} \approx -2y_{\rm tSZ} \,. \tag{1.32}$$

This is the commonly used expression for the temperature variation due to the tSZ effect. By rewriting using the explicit expression for $y_{\rm tSZ}$ one obtains the usual formula

$$\frac{\Delta T_{\rm tSZ}}{T_{\rm CMB}} = -2\sigma_{\rm T}\int \frac{k_{\rm B}T_{\rm e}}{m_{\rm e}c^2}\, n_{\rm e}\, {\rm d}l \,. \tag{1.33}$$

For a typical cluster the brightness change through its centre caused by the tSZ effect should be $\Delta T \approx -0.68$ mK at low frequencies (of order of 100 GHz).

When the condition $x^2 y < 1$ does not apply, the equation (1.20) has to be solved exactly. The solution can be written as

$$n(\nu, y) = \int_{-\infty}^{\infty} P_{\rm K}(s) n(\nu_0, 0)\, {\rm d}s \,, \tag{1.34}$$

in which the Kompaneets scattering kernel is of Gaussian form

$$P_{\rm K}(s) = \frac{1}{\sqrt{4\pi y}} \exp\left(-\frac{(s+3y)^2}{4y}\right) , \tag{1.35}$$

where s is the the logarithmic frequency shift defined above in equation (1.11). The difference between the scattering kernels (1.14) and (1.35) is small in the non-relativistic case but becomes significant for mildly relativistic electrons that are important in most cases, and can became large in regions where the electrons become more relativistic as will be discussed in more detail in Section 1.5 Chapter 1.

1.4 Kinematic Sunyaev-Zel'dovich (kSZ)

Although early work by Sunyaev and Zel'dovich concentrated on the tSZ effect, a second effect might also occur. This is the kinematic SZ (kSZ) effect, which is a result of the bulk motion of clusters or any virialised mass of ionised gas, leading to a Doppler shift in the CMB temperature while preserving its black body spectrum.

For an observer in the rest frame of the CMB, the photon occupation number has the equilibrium form

$$n(x) = \frac{1}{e^x - 1}\,. \tag{1.36}$$

The occupation number in a frame moving with peculiar velocity $v_\parallel$ along the line of sight away from the observer is then

$$n(x_1) = \frac{1}{e^{x_1\gamma_\parallel(1-\beta_\parallel\mu_1)} - 1}\,, \tag{1.37}$$

where $\beta_\parallel = v_\parallel/c$ with corresponding Lorentz factor $\gamma_\parallel$, $\mu_1 = \cos\theta_1$ is the direction cosine of photons arriving at a scattering centre relative to the line-of-sight and measured in the frame of the moving scattering medium, and $x_1 = h\nu_1/k_\mathrm{B}T_1$ is the dimensionless frequency in the frame of the scattering medium with $T_1 = T_{CMB}(1+z_H)$ temperature of the CMB as seen by an observer at rest in the Hubble flow near the scattering gas particles and z_H the cosmological redshift. The relation between the photon frequencies ν_1 and ν as seen respectively from the moving and the CMB reference frames is given by $\nu_1 = \gamma_\parallel(1+\beta_\parallel)\nu$, since the observer at rest sees the scattered photons along the line-of-sight, where the direction cosine of scattered photons with respect to the line-of-sight is $\mu = 1$.

It is possible to derive the intensity for the scattered radiation by the electron bulk flow either from the Boltzmann equation (Phillips 1995) or from the radiative transfer equation (Birkinshaw 1999). The Boltzmann equation for a single scattering centre in a cluster medium with peculiar velocity $v_\parallel$ reads

$$\frac{\mathrm{d}n(\theta, x_1)}{c\mathrm{d}t} = \int \frac{\mathrm{d}\sigma}{\mathrm{d}\Omega_1}\big(n(\theta_1, x_1) - n(\theta, x_1)\big)\mathrm{d}\Omega_1\,, \tag{1.38}$$

where the differential cross-section $\mathrm{d}\sigma/\mathrm{d}\Omega$ is given by the classical Thomson expression (1.8) with $\phi_{12} = \theta_1$. Expressing the solid angle as $\mathrm{d}\Omega_1 = -\mathrm{d}(\cos\theta_1)\mathrm{d}\phi_1 = -\mathrm{d}\mu_1\mathrm{d}\phi_1$ (the negative sign indicates propagation of scattered photons towards the observer, i.e. opposite to the line-of-sight direction) and integrating over $\mathrm{d}\phi_1$ one gets

$$\frac{\mathrm{d}n(\mu, x_1)}{c\,\mathrm{d}t} = \int_{-1}^{1} \frac{3}{8}\sigma_\mathrm{T}(1+\mu_1^2)n(\mu, x_1)\left(\frac{n(\mu_1, x_1)}{n(\mu, x_1)} - 1\right)\mathrm{d}\mu_1\,. \tag{1.39}$$

In order to rewrite equation (1.39) for the whole cluster, all the scattering centres have to be taken into account, thus it has to be multiplied by the electron number density $n_\mathrm{e}(l)$ and integrated over the path length along the line-of-sight l. One finally obtains that the

(finite) change in number density is proportional to the optical depth $\tau_e = \int n_e(l)\sigma_{\rm T}{\rm d}l$ and given by

$$\frac{\Delta n(\mu, x_1)}{n(\mu, x_1)} = \tau_{\rm e} \int_{-1}^{1} {\rm d}\mu_1 \frac{3}{8}(1+\mu_1^2) \left(\frac{n(\mu_1, x_1)}{n(\mu, x_1)} - 1 \right) \tag{1.40}$$

for $\mu = 1$ (i.e. the scattered photon has the direction of the line-of-sight), giving

$$\frac{\Delta n(x_1)}{n(x_1)} = \tau_{\rm e} \int_{-1}^{1} {\rm d}\mu_1 \frac{3}{8}(1+\mu_1^2) \left(\frac{e^{x_1\gamma_\parallel(1-\beta_\parallel)} - 1}{e^{x_1\gamma_\parallel(1-\beta_\parallel\mu_1)} - 1} - 1 \right) . \tag{1.41}$$

In terms of the dimensionless frequency x, this equation reads

$$\frac{\Delta n_x}{n_x} = \tau_{\rm e} \int_{-1}^{1} {\rm d}\mu_1 \frac{3}{8}(1+\mu_1^2) \left(\frac{e^{x} - 1}{e^{x_2} - 1} - 1 \right) , \tag{1.42}$$

where $x_2 = x\gamma_\parallel^2(1+\beta_\parallel)(1-\beta_\parallel\mu_1)$. For small $\beta_\parallel$ the integral can be Taylor expanded in powers of $\beta_\parallel$, and the symmetry of the integral assures that only the terms that are even powers of μ_1 contribute to the computation. One finally obtains

$$\Delta n(x) = -\tau_{\rm e}\beta_\parallel \frac{xe^x}{(e^x-1)^2} . \tag{1.43}$$

Recalling that $\Delta I = x^3 \Delta n(x) I_0$, the scattered radiation intensity and temperature variation are

$$\Delta I = -\tau_{\rm e}\beta_\parallel I_0 \frac{x^4 e^x}{(e^x-1)^2} , \tag{1.44}$$

$$\Delta T_{\rm kSZ} = -\tau_{\rm e}\beta_\parallel T_{\rm CMB} \frac{x^2 e^x}{(e^x-1)^2} . \tag{1.45}$$

In the Rayleigh-Jeans limit $x \to 0$ the spectral form (1.45) yields a pure thermal distortion of magnitude given by

$$\frac{\Delta T_{\rm kSZ}}{T_{\rm CMB}} \approx -\tau_e \frac{v_\parallel}{c} = y_{\rm kSZ} . \tag{1.46}$$

that is, the emergent spectrum is still described completely by a Planck spectrum, but at a slightly different temperature, lower (higher) for positive (negative) peculiar velocities. One of the most interesting outcomes of kSZ is that it provides a method to obtain the component of the peculiar velocity on the line of sight of objects at large distances and these motions place strong constraints on the dynamics of structure formation. For typical clusters structure and motion the brightness change through its centre caused by the kSZ effect should be $|\Delta T| \approx 0.008$ mK at low frequencies.

Because of the small amplitude and no distinctive frequency signature, the kSZ effect is significantly harder to detect than the tSZ effect. Moreover, the kSZ signal is challenging to extract from the CMB because positive or negative signals occur with equal probability and a naïve stacking or cross-correlation analysis will therefore lead to a large cancellation of the signal.

1.5 Relativistic corrections

As discussed above, the tSZ derivation is based on a solution to the Kompaneets equation, a non-relativistic diffusion approximation. For mildly relativistic electrons, the Kompaneets description becomes insufficiently accurate at high frequencies. With ICM temperatures in the range 3-15 keV, the electron velocities are relativistic and the Kompaneets approximation is not valid; the Kompaneets kernel (1.35) must be replaced by a Maxwellian distribution (1.14) yielding to cumbersome integrals. Nonetheless, the Kompaneets treatment provides an adequate description of the spectral change at low frequencies, in the Rayleigh–Jeans regime. In addition, the full relativistic calculations yielding the optical depth demands the Klein-Nishina cross-section, equation (1.7), which decreases as frequency increases. Thus, being relativistic electrons less efficient scattering centres, the cluster will have a lower optical depth and consequently a lower Comptonisation parameter y.

Overall, the relativistic corrections cause a broadening of the tSZ signal; the radiation intensity change decreases for $x \leqslant 8.0 - 8.4$ and increases at higher frequencies. The higher the gas temperature, the higher is the deviation in the Wien region. Another important consequence of the relativistic treatment is the shift of the value of the crossover frequency, which moves to higher values with increasing temperature T_e, while in the non-relativistic description it is $x_0 = 3.83$ and independent of T_e. Relativistic corrections to tSZ effect for a massive cluster with $k_\mathrm{B}T_\mathrm{e} \approx 10$ keV, are of the order of a few percent in the Rayleigh-Jeans side of the spectrum, while the deviation from the crossover frequency is linear in $k_\mathrm{B}T_\mathrm{e}/m_\mathrm{e}c^2$ and corrections are more substantial.

Relativistic corrections to the kSZ are due to the Lorentz boost to the electrons provided by the cluster bulk velocity. The leading term is of order $(k_\mathrm{B}T_\mathrm{e}/m_\mathrm{e}c^2)\beta_\parallel$ and for a cluster with $T_\mathrm{e} \approx 10$ keV moving at 1000 km s^{-1} the correction to the non-relativistic effect is of a few percent. As with the tSZ relativistic corrections for kSZ lead to a broadening and systematic shift of the signal to higher frequencies.

The effects of relativistic corrections are shown for $T_\mathrm{e} = 20$ keV and $T_\mathrm{e} = 50$ keV in Figure 1.1.

1.6 Multiple scattering effects

Multiple scattering events inside rich clusters add another correction to the SZ effects. If the scattering is isotropic, subsequent scattering of the single-scattering tSZ signal has a contribution that, to leading order, is suppressed by a factor $\approx 10y$, resulting in a $\approx 0.1\%$ correction. In this case no correction proportional to τ_e arises.

When scattering-induced anisotropy is considered, the spectral dependence of the multiple-scattering signal is modified and a new contribution of order $\tau_\mathrm{e}/20$ relative to the tSZ effect arises, making the correction detectable. The net measurable signal depends explicitly on the medium structure along the line-of-sight, therefore future measurements of the spatial and frequency dependence of the multiple-scattering SZ signal could help reconstructing intracluster medium (ICM) density and temperature profiles.

2 Measurement techniques

In the 20 years following the first papers by Sunyaev and Zel'dovich (Sunyaev & Zel'dovich 1970, 1972) there were only a few firm detections of the SZ effect. The first attempts to measure the tSZ effect were carried resorting to traditional radiometric methods and using existing ground single-dish radio telescopes, operating at frequencies near 15 GHz, and whose size and general purposes made it difficult to perform the optimisations needed for CMB observations.

Furthermore, observations must be conducted on the appropriate angular scales. Galaxy clusters have a characteristic scale size of order a megaparsec, which in case of distant clusters subtends one or a few arcminutes for a reasonable cosmology; low redshift clusters will subtend a much larger angle (e.g. the angular extent of the Coma cluster ($z = 0.024$) is of order a degree).

Each angular scale poses specific observational difficulties due to contamination with other astronomical sources or to ground pick-up and the Earth's atmospheric variations. The latter leads to inevitable offsets when performing differential measurements toward widely separated directions on the sky in order to observe extended low–surface brightness objects.

2.1 Sources of contamination and confusion

In designing an instrument for SZ effects observation, astronomical sources that could lead to possible contamination and confusion need to be taken into account.

One such source is the primary anisotropy of the CMB itself. It must be accounted for when targeting nearby clusters with angular extents larger than a few arcminutes, whereas on the extension scales of distant clusters, that is less than a few arcminutes, the intrinsic CMB anisotropy is considerably damped. The spectrum of the primary anisotropies is identical to that of the kinematic component of the SZ effect, and, therefore, they limit the accuracy with which cluster peculiar velocities can be determined and in order to separate the two it is necessary to rely on the very small spectral distortions of the kSZ effect due to relativistic effects.

Historically, the major source of contamination in the measurement of the SZ effect has been radio point sources, which, if located along the line of sight to the cluster, contaminate the SZ signal. Radio point sources are variable, with timescales that vary at different frequencies, and therefore must be monitored.

At frequencies near the null of the tSZ effect and higher, dust emission from extragalactic sources as well as dust emission from our own galaxy must be considered.

2.2 Single-dish photometry

As aforementioned pioneering work on the SZ effect made use of preexisting single-dish radio telescopes relying on radiometers which work best on the lower band of the SZ spectrum. These telescopes tend to have beam-sizes of a few arcminutes in the microwave region, a fairly good match to the angular sizes of moderately distant clusters.

Being ground based experiments the major disturbance for observations is the Earth's atmosphere opacity. For example at 20 GHz, in good conditions, its signal would be of order 3K, several thousand times larger than the SZ effects, therefore it must be removed to a part in 10^5 if precise measurements of SZ effects are to be made.

Sensitive observations using single-dishes always rely on some differencing scheme in order to reduce unwanted signals from the atmosphere or pick-up signals from the ground. The simplest differencing scheme consists in position-switching the beam of the telescope between the direction of the observing area and a reference direction well away from the signal of interest. The radiometric signals in these two directions are then subtracted. A similar technique consists in beam-switching: the signals of the two beams are measured many times per second, to yield an "instantaneous" sky signal. On a slower timescale the telescope is position-switched, so that the sky patch being observed is moved between one beam and the other. An alternative strategy is to perform a drift or driven scanning of the sky either allowing the sky to drift through the beam, or driving the telescope so that the beam is moved from the reference direction across the position of the target. Of all the mentioned techniques, the latter is the least efficient because many scans are needed to average out the atmospheric noise and because much of the observing time is spent outside of the target region.

Early observations made at centimetre wavelengths have been plagued by systematic errors that led to irreproducible and inconsistent results. The first claim of detection of the tSZ decrement signature was made by Parijskij in 1973 but the result was not reproducible. Afterwards other successful detections using beam switching techniques were made: Gull and Northover (1976), Lake and Partridge (1977), and especially important in building confidence in the technique is the work of Birkinshaw et al. (1978).

In order to separate the thermal and kinematic components of the SZ effect using their different spectral shapes it is necessary to perform measurements of the tSZ as an increment, outside the Rayleigh-Jeans part of the spectrum. Unlike radiometers that perform well at low frequencies, thermal detectors such as bolometers are intrinsically "broadband" instruments and allow higher sensitivities on a broad frequency range, in particular in the range of frequencies where the tSZ increment resides. Considering however the varying opacity of the atmosphere, namely its increase at higher frequencies that compromises the measure of the increment, it is essential for these detectors that telescopes are positioned on high sites with stable atmospheres and exceptionally low precipitable water vapour.

Accordingly, the first detection of tSZ as an increment was carried out by PRONAOS (Serra et al. 1998) a stratospheric balloon-borne experiment, which together with data from the Sunyaev-Zeldovich Infrared Experiment (SuZIE; Holzapfel et al. 1997) and Diabolo (Benoît et al. 2000) experiments, gave a complete picture of the spectral energy distribution from far-infrared to millimetre wavelengths of the diffuse emission toward a cluster of galaxies (Lamarre et al. 1998).

In the late two-thousands the South Pole Telescope (SPT), using an array of superconducting bolometers (transition edge sensors TESs), and the Atacama Cosmology Telescope (ACT), using the Millimeter Bolometer Array Camera (MBAC; Niemack et

al. 2008), obtained sufficiently high mapping speeds to detect previously unknown clusters in wide-field surveys based on their tSZ effect signals (Staniszewski et al. 2009, Menanteau et al. 2010). Subsequent to these ground-based surveys, the Planck space observatory surveyed the full sky in 9 photometric bands, chosen with the tSZ effect in mind, spanning the range 30–850 GHz and delivering a large all-sky sample of SZ-selected clusters. Three bands (30, 44, and 70 GHz) are observed by the Low Frequency Instrument (LFI; Bersanelli et al. 2010), which consists in arrays of cryogenically cooled radiometers; six frequency bands (from 100 to 857 GHz) are instead scanned by the High Frequency Instrument (HFI, Lamarre et al. 2010) consisting in arrays of bolometer detectors.

Subarcminute angular resolution at millimetre wavelengths is challenging for space experiments, as the size of the primary mirror strongly drives their cost. Planck's best angular resolution of $5'$ is lower by a factor of ~ 5 than that of contemporary bolometer arrays used to study the SZ effect from the ground. Therefore Planck is less sensitive to lower mass clusters than many ground-based experiments, and it is not suitable to study the details of the cluster gas profile.

The first detection of the kSZ signal (Hand et al. 2012) was performed in a statistical manner, combining ACT high-resolution microwave sky maps with clusters surveys and measuring the mean pairwise velocity, an estimator that is sensitive to the gravitational infall of pair of optically identified clusters and that will be discussed in details in the next paragraph.

Whereas the first kSZ measurements in a single cluster were performed towards MACS J0717.5+3745 (Mroczkowski et al. 2012, Sayers et al. 2013) using data collected by MUSTANG bolometer array (Dicker et al. 2008) on the Green Bank Telescope (GBT), along with data from Bolocam (Haig et al. 2004) from the Caltech Submillimeter Observatory (CSO). MACS J0717.5+3745 ($z = 0.55$) is a triple-merger system comprising four distinct, optically detected subclusters, known to present exceptionally large relative line of sight velocities ($\beta \approx 0.01$) and appears to be a compact source (a few arcminutes) making it an excellent target for kSZ measurements. The first resolved map of the kSZ signal in MACS J0717.5+3745 (Figure 1.2; Adam et al. 2017) was obtained using a Kinetic Inductance Detector (KID) array installed on the Institut de Radio Astronomie Millimétrique (IRAM) 30 m telescope, called New IRAM Kinetic inductance detector (KID) Arrays (NIKA; Monfardini et al. 2011). The sensitivities that NIKA is able to obtain in the two frequency channels used for observations (150 GHz and 260 GHz) reach $18''$ and $12''$ respectively.

The main advantage of using bolometers lies in the large mapping speed they provide making them the preferred option especially in the case of wide-field SZ surveys.

While there are prospects of far larger detector counts with improved mapping speeds and ability to recovered larger angular scales when using advancements in detector technologies, particularly KIDs coupled to wide field of view telescopes, there is no immediate prospect for the larger telescope apertures (> 100 meters) required for substantial gains in angular resolution. For that, an interferometer is required.

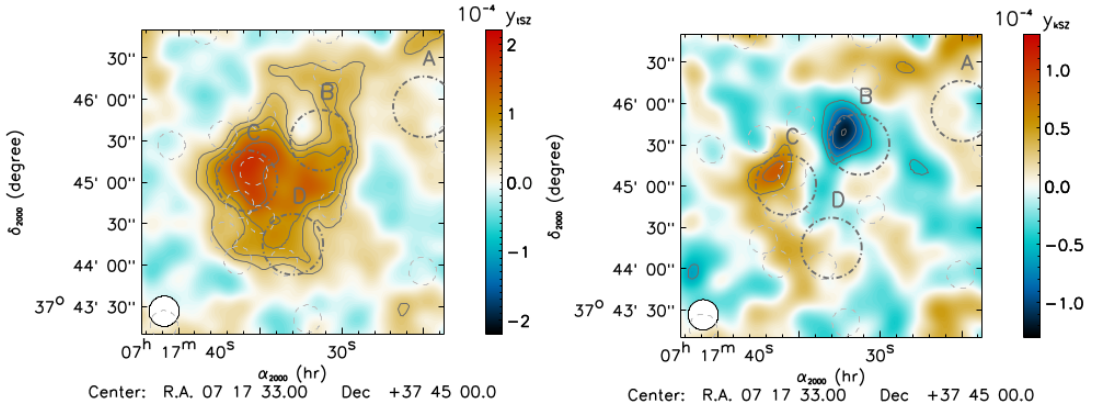

Figure 1.2: Reconstructed maps of the tSZ effect, $y_{\rm tSZ}$ (left), and the kSZ effect, $y_{\rm kSZ}$ (right) combining NIKA 150 and 260 GHz channels, with contours showing the significance in units of standard deviation σ, starting from $\pm 2\sigma$. The map effective resolution, $22''$, is shown as a white circle on the bottom left corner. Subcluster regions are represented in grey. The positions of the identified point sources, are represented in light grey (Adam et al. 2017).

2.3 Interferometry

Photometric observations are excellent for large-scale surveys of clusters of galaxies but provide only modest angular resolutions on the sky. The stability and spatial filtering inherent to interferometry provide a powerful method to make high quality images of the SZ effect, without the requirement of building large aperture elements. Such images are valuable for making detailed comparisons with X-ray images, and can also obtain accurate measures of SZ effects while avoiding some of the systematic difficulties of single-dish observations. One of the main systematics arises from the atmospheric signal, which, being uncorrelated, gets naturally filtered out by interferometric arrays.

The spatial filtering provided by interferometers with a wide range of baselines allows the emission from radio point sources to be separated from the one of SZ nature: the longer baselines correspond to small angular scales, where (angular scales $\lesssim 10''$) the SZ effect contributes very little flux and the signal is dominated by the flux of radio point sources, while the shorter baselines contain both the radio source signal and the SZ signal. Nearly simultaneous monitoring of radio point sources is important, as they are often variable. It provides better source subtraction from short-baseline data, allowing the construction of source-free maps of the sky where the SZ signal can be searched for.

Interferometers offer an ideal way to achieve high brightness sensitivity for extended low-surface brightness emission. However, most interferometers were not designed with this purpose in mind, they have been traditionally built to be maximally sensitive to small-scale emission. Therefore specific interferometric systems have been built in order to obtain SZ imaging.

The first interferometric detection of tSZ (Jones et al. 1993) was obtained with

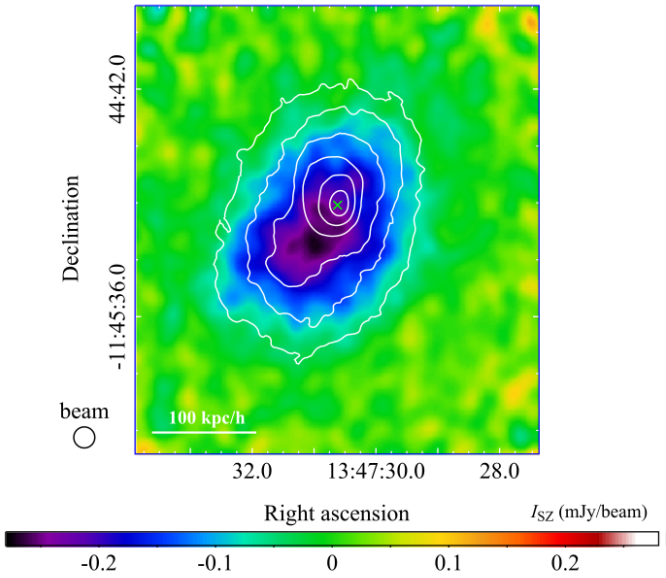

Figure 1.3: ALMA+ACA tSZ map of RX J1347.5-1145 ($z = 0.45$) with X-ray contours overlaid, showing an offset between the X-ray and tSZ surface brightness distributions (Ueda et al. 2018).

the Ryle Telescope at 15 GHz. This interferometer was obtained with the 5 Kilometer Array, consisting of eight 13 m telescopes. Afterwards other detections were obtained at 30 GHz using the Owens Valley Radio Observatory (OVRO; Birkinshaw & Hughes 1994) and the Berkeley-Illinois-Maryland Association (BIMA; Dawson et al. 2001) millimetre-wave arrays. Although the first high-spatial resolution SZ images were produced by the Diabolo bolometric camera on the IRAM 30-meter telescope with a $\approx 20''$ resolution, in the same years OVRO/BIMA were able to obtain the same resolution in some of their interferometric images.

Further improvements on resolution and spatial filtering were obtained with the Atacama Large Millimeter/Submillimeter Array (ALMA). ALMA is an observatory consisting of 2 arrays suitable for SZ detection: fifty 12-meter antennas (usually called "ALMA"), twelve 7-meter antennas known as the Atacama Compact Array (ACA). The best imaging power comes from ALMA main array due to the large collecting area, great spatial filtering (1225 possible baselines) and high resolution up to $3.5''$, however it has a small primary beam and recovers scales $\sim 0.5'$ (much smaller than the typical extents of massive galaxy clusters at any z) at its lowest frequency. ACA functions in a more compact configuration and, due toits smaller elements, has a primary beam larger than the one of ALMA, but it covers a smaller collecting area, has a lower resolution $\sim 13''$, less spatial sampling (only 66 baselines), making imaging more challenging. An example of resulting ALMA+ACA tSZ map is shown in Figure 1.3.

These improved interferometric instruments, while not as fast as bolometric arrays

are able to survey deeper and provide more detailed imaging. In particular, the high resolution and deep imaging provided by future arrays, combining bolometric cameras and interferometric layouts, will provide a valuable tool for investigating cluster structure and its evolution. Such studies are necessary before the full potential of large SZ surveys for cosmology can be realised.

2.4 Estimators for kSZ extraction

While for detecting tSZ averaging its signal is sufficient, in the case of kSZ due to its changing sign, averaging over many sources leads to signal cancellation. To remedy this, the extraction of the kSZ effect can be performed using various approaches: applying a pairwise estimator combining information on the relative gravitational infall of pairs of clusters with their kSZ signal estimates, or by cross-correlating a CMB map with a (observed or reconstructed) velocity field.

Pairwise estimator

Many pairwise estimators have been proposed. One of the most convenient is the one by Ferreira et al. (1999), which relies directly on peculiar velocity samples. Since one observes only the line-of-sight component of the peculiar velocity rather than the full three-dimensional velocity, it is useful to express the estimator in terms of the mean difference between radial velocities of a pair of galaxies, with weights depending only on line-of-sight quantities. The pairwise velocity estimator $\hat{v}_{\rm pair}(r)$ built upon the peculiar velocities $\mathbf{v}_i$ of individual objects located at $\mathbf{r}_i$ in the sky is given by

$$\hat{v}_{\rm pair}(r) = \frac{\sum_{i<j} (\hat{\mathbf{r}}_i \cdot \mathbf{v}_i - \hat{\mathbf{r}}_j \cdot \mathbf{v}_j)\, c_{ij}}{\sum_{i<j} c_{ij}^2}, \tag{1.47}$$

where the weights are given by $c_{ij} = \hat{\mathbf{r}}_{ij} \cdot \frac{\hat{\mathbf{r}}_i + \hat{\mathbf{r}}_j}{2}$, and $\mathbf{r}_{ij} \equiv \mathbf{r}_i - \mathbf{r}_j$ denoting the mean positions of couple i-j, $|\mathbf{r}_{ij}| = r$. Temperature decrease due to kSZ is finally

$$\delta T_{\rm p}(r) \simeq \frac{\tau_{\rm e}}{c} T_{\rm CMB} v_{\rm pair}(r), \tag{1.48}$$

where $v_{\rm pair}(r)$ is the mean relative pairwise velocity of clusters estimated using equation (1.47). If two galaxy clusters are moving towards (apart from) each other, their contribution $\hat{v}_{\rm pair}(r)$ will be negative (positive).

As the kSZ effect provides a proxy for the line-of-sight velocity, the same estimator can be applied to kSZ temperature maps and yield an estimator for temperature variations,

$$\delta\hat{T}_{\rm p}(r) = -\frac{\sum_{i<j} [T(\hat{\mathbf{n}}_i) - T(\hat{\mathbf{n}}_j)]\, c_{ij}}{\sum_{i<j} c_{ij}^2}. \tag{1.49}$$

Any signal associated with individual clusters, like the tSZ effect, will average to zero as long as it does not depend on the relative distance between cluster pairs. Redshift-dependent signals are not ruled out by the estimator and can be confused with the cluster kSZ signal (such as infrared emission from galaxies in the cluster, radio sources emissions, and small variations of the tSZ signal due to evolution of the cluster mass and temperature). However, these effects can be accounted for by correcting the temperature estimates by a redshift-averaged microwave temperature around clusters at a given redshift z_i. The averaged temperature $\overline{T}_{\rm AP}(z_i, \sigma_z)$ is obtained by weighting the kSZ temperature data measured from all clusters by a Gaussian of width σ_z centred on z_i (Hand et al. 2012; Planck Collaboration XXXVIII 2015),

$$\overline{T}_{\rm AP}(z_i, \sigma_z) = \frac{\sum_j T_{\rm AP}(\hat{\mathbf{n}}_j) \exp\left(-\frac{(z_i - z_j)^2}{2\sigma_z^2}\right)}{\sum_j \exp\left(-\frac{(z_i - z_j)^2}{2\sigma_z^2}\right)}\,, \tag{1.50}$$

where $T_{\rm AP}(\hat{\mathbf{n}}_i)$ corresponds to the temperature estimates at the position of the ith cluster centred in $\mathbf{n}_i$ obtained by applying an aperture photometry (AP) filter. The AP method consists in averaging the value of the pixels within a disk of radius $\theta_{\rm disk}$, and correcting for contribution from larger scales by subtracting the average of the pixels in $\theta_{\rm disk} < \theta < \sqrt{2}\theta_{\rm disk}$. This corresponds to integrating the temperature map over a compensated filter

$$W(\theta) = \frac{1}{\pi\theta_{\rm disk}^2} \cdot \begin{cases} 1 & \text{if } \theta < \theta_{\rm disk} \\ -1 & \text{if } \theta_{\rm disk} < \theta < \sqrt{2}\theta_{\rm disk} \\ 0 & \text{if } \theta > \sqrt{2}\theta_{\rm disk} \end{cases}, \tag{1.51}$$

such that $\int W(\boldsymbol{\theta})\,\mathrm{d}\boldsymbol{\theta} = 1$. The relative kSZ temperature estimate at the position of the ith cluster is

$$\delta T(\hat{\mathbf{n}}_i) = T_{\rm AP}(\hat{\mathbf{n}}_i) - \overline{T}_{\rm AP}(z_i, \sigma_z) \tag{1.52}$$

and the estimator for the kSZ temperature maps cleared of redshift-dependent signals can be finally rewritten as

$$\delta\hat{T}_{\rm p}(r) = -\frac{\sum_{i<j} [\delta T(\hat{\mathbf{n}}_i) - \delta T(\hat{\mathbf{n}}_j)]\, c_{ij}}{\sum_{i<j} c_{ij}^2}. \tag{1.53}$$

The comparison of the two estimators (1.47) and (1.53) shows that the temperature observations and the estimator for the velocities are indeed linked by equation (1.48).

CMB-velocity cross-correlation

Another strategy to avoid cancellation of the kSZ signal relies on weighting haloes by their velocities obtained using independent estimates. These estimates can be reconstructed from the observed galaxy clusters number overdensity $\delta_{\rm cl}$ on large scales, where

linearised Jeans equation theory is valid, by solving the linearised continuity equation in comoving coordinates

$$\nabla \cdot \mathbf{v} = -Hf\,\frac{\delta_{\rm cl}}{b}\,, \tag{1.54}$$

or equivalently in redshift space

$$\nabla \cdot \mathbf{v} + f\,\nabla \cdot [(\mathbf{v}\cdot\hat{\mathbf{n}})\hat{\mathbf{n}}] = -Hf\,\frac{\delta_{\rm cl}}{b}\,, \tag{1.55}$$

where $f = d\ln D/d\ln a$ is the linear growth rate, i.e., the logarithmic derivative of the linear growth factor $D(a)$ w.r.t. the scale factor a. A linear bias scheme relating $\delta_{\rm cl}$ to the total matter overdensity δ is supposed, namely $\delta_{\rm cl} = b\,\delta$, with bias parameter b estimated from the auto-correlation of the galaxy cluster catalogue. Equation (1.55) (or equivalently equation (1.54)) hands the line-of-sight reconstructed velocity $v_{{\rm rec},i}$ (defined to be positive when pointing away from the observer).

The same AP filter described in the previous section is applied at the position of each galaxy, and yields an estimate δT_i of the kSZ signal from the host halo. In order to compare the AP filter output δT_i and $v_{{\rm rec},i}$ using the relation

$$\frac{\delta T_i}{T_{\rm CMB}} = -\alpha\tau_{{\rm e},i}\frac{v_{{\rm rec},i}}{c}\,, \tag{1.56}$$

it is necessary to estimate the optical depth $\tau_{{\rm e},i}$ of each cluster. It can be obtained by relating the galaxy stellar mass to the total hosting halo mass by assuming cosmological baryon abundance, so that the halo mass is converted into baryon mass. By further supposing baryon full ionisation, the number (mass) of baryons is converted into the number (mass) fraction of free electrons, $f_{\rm free}$. The optical depth obtained is then related to the true one by a factor of $1/f_{\rm free}$, since part of the electrons are in the neutral medium.

The constant α is a linear function of $f_{\rm free}$, with a slope depending on several variables (such as the filter size and shape, the baryon profile, the uncertainties in mass and velocity, etc.) that need to be taken into account to constrain $f_{\rm free}$ but not for the purpose of kSZ signal detection. Finding $\alpha \approx 0$ consistent with zero means no detection of kSZ, while $\alpha \approx 1$ corresponds to a number of free electrons consistent with the cosmological abundance.

3 Derivation of cosmological parameters

The SZ effect provides an exceptional probe for physics beyond the local Universe for it doesn't depend on redshift and hence is not affected by cosmological dimming.

In early stages of CMB study the SZ effect was considered interesting also as proof that the CMB radiation is genuinely a cosmological signal: the appearance of the SZ effect from clusters at high redshift proves that the CMB photons originated beyond that redshift. Thereafter the attention towards the SZ effect has been oriented to estimation of the Hubble constant H_0.

3.1 Measuring H_0 using X-ray and tSZ

The combination of X-ray imaging spectroscopy and millimetric observations of galaxy clusters provides a way to probe H_0 both in early and late stages of the evolution of the Universe (Cavaliere, Danese & de Zotti 1977, 1979; Silk & White 1978). A measure of tSZ signal, which is independent of distance, allows some assessments of the distance to the cluster by comparison with the observed X-ray flux, if one assumption is made about the geometry (symmetry) of the gas distribution.

Only the characteristic scale of the cluster in the plane of the sky is measured, so one must relate the characteristic scales along the line-of-sight and in the plane of the sky, this is done by constructing a model for the cluster gas distribution. The most used and convenient model of the cluster atmosphere geometry is the spherical isothermal β-model by Cavaliere & Fusco-Femiano (1976, 1978), for which the free electron number density at distance $\mathbf{r}$ from the centre is

$$n_{\mathrm{e}}(r) = n_{\mathrm{e}0}\left(1 + \frac{r^2}{r_{\mathrm{c}}^2}\right)^{-\frac{3}{2}\beta} . \tag{1.57}$$

Here $n_{\mathrm{e}0}$ is the electron number density at the centre of the cluster, r is the radius measured from the centre of the cluster, r_{c} is the core radius of the intracluster medium (ICM) as deduced from the X-ray data, and β is a real-valued index. With this model, the cluster extent along the line-of-sight is the same as that in the plane of the sky. Most clusters are dynamically young, aspherical, and do not appear circular in radio, X-ray, or optical observations. The effects of asphericity contribute significantly to the in tSZ and X-ray derived distance uncertainty for each cluster, however when one considers a large unbiased sample of clusters with random orientations, the errors due to imposing a spherical model are expected to cancel, resulting in a precise determination of H_0.

The distance to the cluster is determined by exploiting the different density dependencies of the tSZ and X-ray signals. The tSZ signal is proportional to the first power of the electron number density

$$\Delta T_{\mathrm{tSZ}} = f(x)\, T_{\mathrm{CMB}} \int \sigma_{\mathrm{T}}\, n_{\mathrm{e}} \frac{k_{\mathrm{B}} T_{\mathrm{e}}}{m_{\mathrm{e}} c^2}\, \mathrm{d}l\,, \tag{1.58}$$

that is the pressure integrated along a given line-of-sight through the galactic cluster, where $f(x)$ is given in expression (1.1). The distance dependence is made explicit with the substitution $\mathrm{d}l = D_{\mathrm{A}}\mathrm{d}\zeta$, where D_{A} is the angular-diameter distance of the cluster and ζ is the angular size down the line-of-sight. Equation (1.58) then gives

$$\begin{aligned}
\Delta T_{\mathrm{tSZ}} &= f(x)\, T_{\mathrm{CMB}} D_{\mathrm{A}} \int \sigma_{\mathrm{T}}\, n_{\mathrm{e}} \frac{k_{\mathrm{B}} T_{\mathrm{e}}}{m_{\mathrm{e}} c^2}\, \mathrm{d}\zeta \\
&= f(x)\, T_{\mathrm{CMB}} y_0 \left(1 + \frac{\theta^2}{\theta_{\mathrm{c}}^2}\right)^{\frac{1}{2}-\frac{3}{2}\beta} \qquad (1.59) \\
&= \Delta T_0 \left(1 + \frac{\theta^2}{\theta_{\mathrm{c}}^2}\right)^{\frac{1}{2}-\frac{3}{2}\beta} , \qquad (1.60)
\end{aligned}$$

where $\theta_{\rm c} = r_{\rm c}/D_{\rm A}$ is the angular core radius of the cluster and y_0 is the central value of the Comptonization parameter given by

$$y_0 = n_{\rm e0}\,\sigma_{\rm T}\frac{k_{\rm B}T_{\rm e0}}{m_{\rm e}c^2}D_{\rm A}\theta_{\rm c}\sqrt{\pi}\frac{\Gamma\left(\frac{3}{2}\beta-\frac{1}{2}\right)}{\Gamma\left(\frac{3}{2}\beta\right)}\,, \tag{1.61}$$

written in terms of the Euler gamma function $\Gamma(x) \equiv \int_0^\infty t^{x-1}e^{-t}{\rm d}t$. X-ray emission from the ICM has a different dependence on the density. Arising from two-body collisions, the X-ray surface brightness is proportional to the square of the electron number density,

$$S_{\rm X} = \frac{1}{4\pi(1+z)^3}D_{\rm A}\int n_{\rm e}^2\Lambda_{\rm e}{\rm d}\zeta \tag{1.62}$$

$$= S_{\rm X0}\left(1+\frac{\theta^2}{\theta_{\rm c}^2}\right)^{\frac{1}{2}-3\beta}\,, \tag{1.63}$$

where $\Lambda_{\rm e}$ is the X-ray spectral emissivity of the ICM and $S_{\rm X0}$ is the X-ray surface brightness at the centre of the cluster given by

$$S_{\rm X0} = \frac{\Lambda_{\rm e0}n_{\rm e0}^2}{4\pi(1+z)^3}D_{\rm A}\theta_{\rm c}\sqrt{\pi}\frac{\Gamma\left(3\beta-\frac{1}{2}\right)}{\Gamma\left(3\beta\right)}\,. \tag{1.64}$$

An absolute angular diameter distance is then found by fitting the X-ray and tSZ effect data to models of the form given by expressions (1.60) and (1.63), and solving for $D_{\rm A}$ by eliminating $n_{\rm e0}$

$$D_{\rm A} \propto \frac{(\Delta T_0)^2}{S_{\rm X0}}\frac{\Lambda_{\rm e0}}{T_{\rm e0}^2}\frac{1}{\theta_{\rm c}}\,. \tag{1.65}$$

This method can effectively provide distances to high redshift galaxy clusters as it does not rely on on the extragalactic distance ladder, but rather only on properties of highly ionised plasma. The theoretical expression for $D_{\rm A}$ can be obtained using Mattig formula (Mattig 1958)

$$D_{\rm A} = \frac{c}{H_0 q_0^2}\frac{q_0 z + (q_0-1)(\sqrt{1+2q_0 z}-1)}{(1+z)^2}\,, \tag{1.66}$$

thus H_0 can be determined from a comparison of the two expressions (1.65) and (1.66). Dependence on the deceleration parameter q_0 can be neglected for $z \ll 0.2$, where $D_{\rm A} \approx cz/H_0$. For higher redshifts $D_{\rm A}$ is obtained under some assumption about q_0. The relevant dependence of $D_{\rm A}$ on q_0 can, in principle, be used to determine q_0, but the observational challenges that this outcome poses only allow a distinction between extreme values of q_0. For example, if $D_{\rm A}$ of a cluster at $z \sim 1$ is determined within 25% accuracy, the distinction between extreme open and closed cosmological models can be made at the σ statistical significance level.

The major systematic effect that limit the precision of H_0 is the absolute calibration of ICM temperatures measured from X-ray data. Another challenge, particularly in the case of an unresolved clusters, is the presence of complex thermodynamic structures in merging clusters, as well as the possibility of biases in X-ray measurements of gas density at large radii due to clumping, which impede the use of simple electron density profiles such as the β-model, equation (1.57).

3.2 Cosmology from tSZ clusters counts

The study of the spatial distribution of clusters of galaxies and their evolution with redshift has played, and is still playing, a significant role in the development of cosmological tests, being the spatial statistics (in particular counts and two-point correlation functions) sensitive to the cosmic matter density $\Omega_{\rm m}$ and the rms-mass variance in spheres of radius 8 h^{-1}Mpc. Namely the number of clusters expected to be found in tSZ surveys depends sensitively on the assumed cosmology.

Evidence both from observation and from numerical simulations suggests that the total tSZ flux, or integrated Comptonisation parameter, $Y_{\rm tSZ} = \int y_{\rm tSZ}\,{\rm d}\Omega \propto D_{\rm A}^2 \int P_{\rm e}{\rm d}V$, is expected to tightly correlate with mass (Planck collaboration XX 2013). This strong correlation allows the comparison of cluster counts obtained with large-scale tSZ surveys with expected values obtained by theoretical modelling of cluster mass.

The number density of clusters as function of mass of their dark matter halo hosts and redshift is described by the so-called halo mass function, which can be derived by applying the statistics of peaks in a Gaussian random field (e.g. following the standard Press & Schechter 1974, or extended Press & Schechter formalism by Seth & Tormen 1999), or fitting large cosmological N-body simulations (e.g. Tinker et al. 2008; Watson et al. 2013). In full generality it can be written as

$$\frac{{\rm d}n(M,z)}{{\rm d}M} = -\phi(\sigma)\frac{\overline{\rho}_m}{M^2}\,\frac{{\rm d}\ln\sigma(M,z)}{{\rm d}\ln M}\,, \tag{1.67}$$

where $\overline{\rho}_m(z) \equiv \Omega_m \rho_{\rm crit}(z) = \overline{\rho}_m(0)(1+z)^3$ is the mean background matter density at the epoch of the analysis, with $\rho_{\rm crit} = 3H^2(z)/8\pi G$ the critical density, $\sigma^2(M,z) \equiv \langle M^2\rangle - \langle M\rangle^2 = \sigma^2(M)D^2(z)$ is the mass variance, with $\sigma^2(M)$ its current value and $D(z)$ the linear growth function. The so called multiplicity function $\phi(\sigma)$ is proportional to $e^{-\delta_c^2/2\sigma^2}$, explaining the exponential suppression of the abundance of very massive objects since $\sigma(M) \sim M^\alpha$ with negative power ($\alpha \sim -4/3$ in SCDM). The abundance suppression is also sensitive to $D(z)$, thus it depends on cosmological parameters.

The primary motivation for large surveys for galaxy clusters using the tSZ effect is to obtain a cluster catalogue with a well-understood selection function that is a very mild function of cosmology and redshift. However, selection biases always occur. Arguably an alternative way of conducting large-scales analysis, less sensitive to selection biases, is using the tSZ power spectrum instead of number counts. The tSZ angular spectrum in the so-called halo formalism is given by

$$C_\ell = f(x)^2 \int_0^{z_{\rm max}} {\rm d}z \frac{{\rm d}V}{{\rm d}z} \int_{M_{\rm min}}^{M_{\rm max}} {\rm d}M \frac{{\rm d}n(M,z)}{{\rm d}M} |\hat{y}_{\rm tSZ}(M,z)|^2\,, \tag{1.68}$$

where $l \simeq 2\pi/\theta$ is the angular mode corresponding to the angular scale θ, $f(x)$ is the spectral signature of tSZ expressed in equation (1.1), $V(z)$ is the comoving volume of the Universe, $\hat{y}_{\rm tSZ}$ is the Fourier transform of the tSZ Comptonisation parameter, and ${\rm d}n(M,z)/{\rm d}M$ the comoving halo mass function. The dependence of the amplitude on

cosmological parameters is well approximated by

$$C_\ell \propto \sigma_8^7 (\Omega_b h)^2 \qquad 0.15 < \Omega_m < 0.4\,, \tag{1.69}$$

$$C_\ell \propto (\Omega_b h)^2 \Omega_m \sigma_8^{6.5\Omega_m^{-0.2} - 0.9\sigma_8} \qquad 0.4 > \Omega_m\,, \tag{1.70}$$

showing the strong dependence on σ_8.

3.3 Cluster gas mass fraction using tSZ

The ICM contains most of the baryons confined to the cluster potential. The gas mass fraction f_g is a reasonable estimate of the baryonic mass fraction of the cluster. It should also be a reasonable approximation of the universal baryon mass fraction $f_\mathrm{b} \equiv \Omega_\mathrm{b}/\Omega_\mathrm{m}$, as long as mass segregation does not occur on the large scales from which massive clusters condense (about 1000 Mpc^3). The gas fraction is actually a lower limit, $f_g \leqslant f_\mathrm{b}$, because a small fraction of baryons ($\approx 10\%$) is likely lost during cluster formation. A measurement of f_b allows for an estimate of Ω_m, given an independent determination of Ω_b.

The gas mass is measured directly by observations of tSZ signal, provided the electron temperature T_e is known. If the gas can be approximated as isothermal, the tSZ signal is proportional to the integrated electron density in a cylindrical volume of fixed radius r, with height given by the cluster width along the line-of-sight delimited by the two distances l_1 and l_2

$$y_\mathrm{tSZ} = \frac{k_\mathrm{B}\sigma_\mathrm{T}}{m_\mathrm{e}c^2}\, T_\mathrm{e} \int_0^r \mathrm{d}r' \int_{l_1}^{l_2} \mathrm{d}l'\, n_\mathrm{e}(l', r') = \frac{k_\mathrm{B}\sigma_\mathrm{T}}{m_\mathrm{e}c^2}\, T_\mathrm{e} N_\mathrm{e}\,. \tag{1.71}$$

Assuming a value for the number of nucleons per electron N_e, the total mass of the ionised phase M_gas can be deduced and it results to be inversely proportional to T_e, $M_\mathrm{gas}^\mathrm{SZ} \propto y_\mathrm{tSZ}/T_\mathrm{e}$.

The total gravitating mass, mainly made of dark matter, can be determined by assuming hydrostatic equilibrium (HSE) and using the distribution of the gas and the electron temperature. The HSE total mass estimate is directly proportional to T_e, $M_\mathrm{HSE} \propto T_\mathrm{e}$. The gas mass fraction then will be

$$f_g = \frac{M_\mathrm{gas}^\mathrm{SZ}}{M_\mathrm{HSE}} \propto \frac{y_\mathrm{tSZ}}{T_\mathrm{e}^2} \tag{1.72}$$

3.4 Clusters peculiar velocity using kSZ

The detection of the kSZ effect has great cosmological value as it provides a unique method to measure large-scale peculiar velocity fields at high redshift. Mass density fluctuations and peculiar velocities both evolve under the effect of gravity in an expanding Universe according to the gravitational instability scenario. As discussed in Section 2.4 Chapter 1, the velocity field $\mathbf{v}$ of clusters is related to the density contrast δ through the linearised continuity equation expressed in comoving coordinates

$$\nabla \cdot \mathbf{v} = -Hf\delta\,. \tag{1.73}$$

The logarithmic linear growth rate is commonly approximated by $f(\Omega) \approx \Omega_m^{0.6}$ (Peebles 1980) and δ is related to σ_8. Thus, peculiar velocities directly probe the mass distribution in the Universe, which reflects the initial conditions and the dynamical evolution of cosmic structures. Hence they can be used to further constrain theories of structure formation and cosmological models.

Alternatively, if the analysed peculiar velocity field is based on estimates of the mean relative pairwise velocities $v_{\rm pair}$, the explicit dependence on cosmological parameters comes from the logarithmic linear growth factor $f(\Omega) \approx \Omega_m^{0.6}$ and from the two-point correlation function $\xi(r)$. For models with Gaussian initial conditions the value of $v_{\rm pair}$ is related to the $\xi(r)$ through (Juszkiewicz, Springel & Durrer 1998)

$$v_{\rm pair}(r) = -\frac{2}{3} H_0 r f \bar{\bar{\xi}}(r)\big(1 + \alpha \bar{\bar{\xi}}(r)\big)\,, \tag{1.74}$$

$$\bar{\xi}(r) = \frac{3}{r^3}\int_0^r \xi(x) x^2 {\rm d}x \equiv \bar{\bar{\xi}}(r)\big(1 + \xi(r)\big)\,, \tag{1.75}$$

where α is a parameter depending on the logarithmic slope of $\xi(r)$. If $\xi(r)$ is a pure power-law ($\xi(r) \propto r^{-\gamma}$)

$$\bar{\xi}(r) = \frac{3\xi(r)}{3-\gamma} \propto \sigma_8^2\,. \tag{1.76}$$

Thus $v_{\rm pair}$ can be expressed in terms of Ω_m through f and σ_8 through $\xi(r)$ and provides an estimate of $\Omega_m^{0.6}\sigma_8^2$ (Ferreira et al. 1999, Peebles 1980).

Classical methods to measure clusters kinematics based on redshift require to subtract the Hubble flow at objects' position in order to obtain their true peculiar velocities. They are therefore limited to small redshifts as the errors increase linearly with distance. Instead, the kSZ effect provides a direct way of measuring peculiar velocities and might be the only way to measure large-scale bulk motions accurately at high redshifts.

Using the kSZ effect to measure the peculiar velocity of a single cluster is especially challenging due to the intrinsic weakness of the signal and the degeneracy of its spectrum with the one of the CMB. Uncertainties on the bulk-flow velocity field by averaging over many clusters are of order several hundred km s^{-1} for low-redshift clusters. Whereas the uncertainty in individual velocity measurements on bright clusters falls between 500 and 1000 km s^{-1}, depending on the cluster core radius. For example Holzapfel et. al (1997) used SuZIE to observe the two clusters Abell 2163 ($z = 0.202$) and Abell 1689 ($z = 0.183$) in three frequency bands (140 GHz, 218 GHz and 270 GHz) covering and bracketing the null of the tSZ spectrum. The constraints obtained on their peculiar velocities are $v_{\rm p} = +490^{+1370}_{-880}$ km s^{-1} and $v_{\rm p} = +170^{+815}_{-630}$ km s^{-1} respectively.

3.5 Constraints on reionisation

The ICM plasma is ionised during the epoch of reionisation (EoR). Thus, the kSZ signal can be decomposed into the "late-time" contribution from $z \lesssim 3$ (discussed until now point) and a "reionisation" contribution from $z \sim 7$, when the ionisation fraction is expected to be inhomogeneous. The contribution arising when the ionisation is complete

is commonly called "homogeneous" kSZ effect (h-kSZ), whereas the contribution arising during the EoR due to the proper motion of reionised bubbles is called "patchy" kSZ (p-kSZ). The latter signal carries information on the EoR as it is sensitive to the reionisation mean redshift $\overline{z}$ and its duration Δ_z. The physical explanation for this sensitivity is that the average proper density of the universe increases with z and the number of ionised bubbles scattering CMB photons depends on Δ_z. Consistently, the angular power spectrum for kSZ then can be split in two terms,

$$D_\ell^{\rm kSZ} = D_\ell^{\rm h-kSZ} + D_\ell^{\rm p-kSZ}\,, \tag{1.77}$$

where $D_\ell = \ell(\ell+1)C_\ell/2\pi$. The two contributions are expected to have a slightly different shape: the p-kSZ power spectrum peaks at a larger angular scale, corresponding to the characteristic bubble size during reionisation, with respect to the one of h-kSZ. Their amplitude depends on cosmological parameters and again especially on σ_8. For $\ell = 3000$ this scaling gives the amplitude $A_{\rm kSZ} \equiv D^{\rm kSZ}_{\ell=3000}$ for the two different anisotropies

$$A^{\rm h}_{\rm kSZ} \propto \tau^{0.44} \tag{1.78}$$

$$A^{\rm p}_{\rm kSZ} \propto \overline{z}\Delta_z^{0.51}\,. \tag{1.79}$$

For $\tau = 0.058 \pm 0.012$ one obtains $A^{\rm h}_{\rm kSZ} \approx 1.79\mu{\rm K}^2$ and $A^{\rm p}_{\rm kSZ} \approx 1.01\mu{\rm K}^2$ (Planck Collaboration XLVII 2016). The h-kSZ signal carries information on the redshift at which the reionisation ended $z_{\rm rei}$, since it depends on the total optical depth τ from the observer located at $z = 0$ to $z_{\rm rei}$; this is clear from equation (1.78) and equation (1.46) rewritten in integral form and making the dependence on z explicit,

$$\frac{\Delta T^h_{\rm kSZ}}{T_{\rm CMB}}(\hat{\mathbf{n}}) = \frac{\sigma_{\rm T}}{c}\int_0^{z_{\rm rei}} {\rm d}z\,\frac{{\rm d}\chi}{{\rm d}z}\frac{n_{\rm e}(z)}{1+z}\,e^{-\tau(z)}\mathbf{v}_{\rm e}\cdot\hat{\mathbf{n}}\,. \tag{1.80}$$

where ${\rm d}\chi$ is the comoving line element, $\mathbf{v}_{\rm e}$ is the free electrons peculiar velocity, and $\hat{\mathbf{n}}$ is the line-of-sight direction, and the optical depth τ is given by

$$\tau = \sigma_{\rm T}\int_0^{z_{\rm rei}} {\rm d}z\,\frac{{\rm d}\chi}{{\rm d}z}\frac{n_{\rm e}(z)}{1+z}\,. \tag{1.81}$$

The h-kSZ power spectrum could therefore be used to measure $z_{\rm rei}$, however the uncertainty on other degenerate cosmological parameters hinders this information.

At least in principle, due to the different angular (l) dependence of the two signals, they can be separated by a precise measurement of the power spectrum on a wide range of angular scales. In practice this is not an easy task since the primary CMB signal is much stronger than that of the kSZ at $\ell < 3000$, while extra-galactic foregrounds dominate at $\ell > 5000$. The observable of the reionisation history that can be probed by CMB data is the total kSZ amplitude $A_{\rm kSZ}$ and the modelled h-kSZ power affects the level of p-kSZ allowed by the data. With more h-kSZ power, less p-kSZ power is allowed. To measure the p-kSZ component of this signal and then constrain $\overline{z}$ and Δ_z, it is therefore vitally important to have a good theoretical understanding of the h-kSZ contribution. In this work the focus will be on the kSZ signal imprinted on CMB photons at late times, nonetheless in order to study the reionization contribution to the signal it is crutial to be able to precisely characterise the post-reionization kSZ effect.

3.6 Intracluster medium substructure

Clusters are not only mass tracers on large-scales, their own substructure is of astrophysical and cosmological interest. In order to tighten the constraints on cosmological parameters from clusters distribution, precise mass estimates are required for cluster surveys. A useful tool to infer these masses comes from the detailed description of the thermodynamic variables profiles, e.g. pressure profiles, and the study of the physical processes involved in mergers of massive clusters as they significantly affect the cluster observables.

Pressure substructures

Pressure substructures, such as for instance shock fronts, are related to gas compression driven by merger events and cosmic accretion. Shock fronts are observable in tSZ high spatial resolution maps due to their pressure jumps from pre-shock and post-shock regions. The linear dependence of tSZ on gas density allows to study shocks in the low density cluster outskirts and since for relatively strong shocks in the hot ICM the post-shock temperature is very high, it falls beyond the spectral window of most X-ray satellites, making tSZ the most suitable method for detecting these substructures.

In addition to shock fronts, other pressure substructures are also found in the ICM. For example tSZ observations of the cluster RX J1347.5-1145 ($z = 0.45$; Ueda et al. 2018) detected an offset between the dense X-ray core and the pressure peak (Figure 1.3), indicating that what was thought to be a dynamically relaxed cool-core cluster is actually an ongoing merger. These tSZ data provided the first direct observational evidence for sub-sonic sloshing motion of the cool core.

Internal gas motion

Alongside tSZ maps, high spatial resolution maps of kSZ can be used to measure the internal bulk and rotational gas motions of the ICM. Measuring, for example, the collision velocity of merging systems provides insights of the cluster physics. This kind of measure is very difficult and ideal targets are one with high merger velocities like MACS J0717.5+3745.

As it will be discussed in more details in the next chapter, adding the polarisation information of the kSZ signal it is possible (at least in principle as this type of measurement is still futuristic) to reconstruct the full 3D bulk and rotational velocity vectors.

4 Polarisation

In addition to modifying the radiation intensity spectrum, the SZ effect also gives rise to a linear polarisation. The comptonisation of CMB photons can lead to a distinct frequency-dependence of the polarised SZ (pSZ). For this the origin of the polarisation plays a crucial role.

The largest pSZ effect is due to the presence of a primordial quadrupole component of CMB anisotropy in the local radiation field at the galaxy cluster location. The second largest pSZ signal is due to multiple scattering of the emerging tSZ and kSZ signals in the same scattering atmosphere. Furthermore Sunyaev and Zel'dovich (1980) highlighted the existence of a polarisation due to the cluster motion transverse to the line of sight with respect to the CMB. Yet another physical mechanism that could lead to polarisation of the SZ signal is associated with anisotropic distribution function of electrons.

To date no polarisation has been detected and even in the future pSZ signals will be challenging to extract due to their intrinsic faintness and the large number of polarised astrophysical signals that could contaminate them. Nevertheless, pSZ signals may provide improvements in detailed studies of ICM structure, and maybe become accessible through stacking analyses.

4.1 Quadrupole anisotropy of the CMB

If a CMB photon incident on a cluster has a quadrupole anisotropy in the plane normal to the line of sight to the cluster, the scattered photon will be linearly polarised. Moreover, the polarisation vector will be determined by the amplitude and orientation of the quadrupole anisotropy of the incident radiation, thus by determining the linear polarisation of the CMB through distant clusters one is measuring independent components of the quadrupole moment of distant observers' surfaces of last scattering. Thus this mechanism could possibly be used to overcome the cosmic-variance limit and to trace the evolution of the CMB quadrupole, provided that measurements could be obtained for a large number of clusters binned in direction and redshift.

In addition to reducing the cosmic variance, the quadrupole moments measured for high redshift clusters (for which the surface of last scattering is smaller than ours) probe smaller scales, comparable to those probed by the observed CMB higher-ℓ moments. Therefore, by observing the redshift dependence of the mean cluster polarisation, one can obtain an independent measure of the shape of the power spectrum.

The polarisation amplitude is $\approx 0.1\tau_{\rm e}Q$ in units of the CMB temperature (Kamionkowski & Loeb 1997, Sazonov & Sunyaev 1999). Here Q is the CMB quadrupole moment at the location of the cluster. The the expected polarisation level for this effect is $50(\tau_{\rm e}/0.01)$ nK for the maximum CMB quadrupole-induced polarisation, too small to expect detection in the near future. Furthermore, the frequency-dependence of this signal is identical to that of the primordial CMB polarisation anisotropies, thus precise knowledge about the cluster location and redshift are required.

4.2 Tangential component of the peculiar velocity

In addition to finding the radial component of the peculiar velocity of a cluster $v_\parallel$, there is the possibility, at least in principle, of also finding the tangential component $v_\perp$ trough the measurement of a polarisation effect of second order in $\beta_\perp = v_\perp/c$. This pSZ effect arises from the fact that in the rest frame of the cluster ionised gas the Planckian form of the CMB spectrum is conserved; however, the temperature of the Doppler shifted

radiation depends on the angle θ between the direction of incidence of a photon and the velocity vector of the cluster. This dependence affects the linear polarisation, which results to be $P_\nu = 0.1\tau_\mathrm{e}\beta_\perp^2$ at low frequencies (Sazonov & Sunyaev 1999). Observations are very challenging as the signal is extremely weak.

4.3 Multiple scattering

Another polarisation effect is connected with multiple consecutive scatterings of a CMB photon within the intracluster gas, i.e. due to a finite optical depth. Although τ_e is small, it is possible that pSZ effects of the order of τ_e^2 may become observable. Indeed, after first scattering in the intracluster medium, the CMB can acquire an anisotropy owing to tSZ and kSZ (due to the component of the cluster velocity along the line of sight) effects. The magnitude of this local anisotropic component is proportional to $(k_\mathrm{B}T_\mathrm{e}/m_\mathrm{e}c^2)\tau_\mathrm{e}$ for tSZ and $\beta_\parallel\tau_\mathrm{e}$ for kSZ.

Second scattering within the ICM will induce pSZ signals of the order $(k_\mathrm{B}T_\mathrm{e}/m_\mathrm{e}c^2)\tau_\mathrm{e}^2$ and $\beta_\perp\tau_\mathrm{e}^2$, where the latter can assume different signs depending on the direction of motion. In the first approximation, the frequency dependence of the two pSZ effects will be the same as that of tSZ or kSZ signals.

4.4 Anisotropy of the distribution function of electrons

The ICM is a weakly collisional plasma and this leads to charged particles having Larmor frequencies exceeding collision frequencies. In such conditions the magnetic moments of particles are conserved between collisions and the evolving magnetic fields or heat fluxes can generate pressure anisotropies. Therefore, thermal velocities of electrons can differ in the directions parallel and perpendicular to the magnetic field, inducing a polarisation pattern in the incident radiation. The signal scales linearly with the optical depth of the anisotropy region, and with the degree of anisotropy itself. It has the same spectral dependence as the kSZ effect polarisation, but can be distinguished by its spatial pattern. The magnitude of the effect is similar to the other pSZ signals.

Since polarisation happens due to weak collisionality, an increase in this due to plasma instabilities will reduce the effect. Thus such pSZ may be an independent probe of the electron collisionality in the ICM, which is one of the key properties of a high-β weakly-collisional plasma from the point of view astrophysics.

Chapter 2

Data simulation and analysis

Measurements of statistics probing the large scale structure are based on galaxy clusters and galaxy catalogues. According to the current picture of cosmological structure formation, every galaxy forms within a host dark matter halo, whose growth over time affects the growth of hosted galaxies and the interaction with other haloes.

Galaxies and galaxy clusters are tracers of dark matter haloes. The advent of massive cluster and galaxy surveys as well as high-resolution cosmological simulations is providing new means to investigate their statistical relationship and evolution. The galaxy–halo connection consists in the multi-variate distribution of galaxy and halo properties that can be derived from both observations and simulations. Individual galaxy properties need then to be related to the total mass of the host halo. This operation can be carried out following various approaches that can be schematically divided into two categories: by empirical modelling, which uses data to constrain a specific set of parameters describing the relation at a given epoch or as a function of time, and physical modelling, which directly simulates or parameterises the physics of galaxy formation such as gas cooling, star formation, and feedback.

Hydrodynamical simulations provide powerful tools to study this relation that connects galaxies and host haloes, as they allow to construct mock catalogues of haloes corresponding to astrophysical objects, such as galaxies or galaxy clusters, based on these models.

1 Hydrodynamical simulations: Magneticum

The understanding of the visible component of the Universe requires the modeling of gravitational interactions and of gas physics. The most explicit way to model galaxy formation is using numerical hydrodynamic techniques, in which the equations of gravity and hydrodynamics are concurrently solved for dark matter and continuous fields representing gas and stars, sampled by pseudo-particles or using grids.

The subgrid model of galaxy formation in a cosmological context, further incorporates feedback processes such gas cooling, stellar-feedback driven winds, and feedback from black holes and supernovae, and in some cases magnetic fields and cosmic rays,

and tracing the properties of dark matter, gas, and stars over time. Although they contain extensive physical prescriptions, hydrodynamic simulations cannot simulate the full range of scales needed for galaxy formation in a cosmological context but need some parameterisations below the resolution scale, generally termed "subgrid physics". Subgrid physics needs to be tuned either through direct tests with observations or by comparison to constraints with empirical models that connect observations to dark matter haloes (Wechsler & Tinker 2018).

This work is based on the Magneticum simulation suite[(1)], which includes one of the largest hydrodynamical simulations performed to date. These simulations are based on `P-GADGET3` (Springel 2005) a state-of-the-art parallel cosmological Tree Particle-Mesh smoothed-particle hydrodynamics (SPH) code.

The simulation cosmological volume used in this work is *Box2*/hr of the Magneticum Pathfinder Simulation set (Hirschmann et al. 2014; Dolag et al. 2015), consisting in a comoving box size of $(352\ h^{-1}\mathrm{Mpc})^3$ simulated with 2×1564^3 particles, adopting a WMAP7 (Komatsu et al. 2011) flat ΛCDM cosmology with $\sigma_8 = 0.809$, $h = 0.704$, $\Omega_m = 0.272$, $\Omega_b = 0.0456$, and power spectral index $n_s = 0.963$. Dark matter particles have a mass of $m_{\mathrm{DM}} = 1.3 \times 10^{10} M_{\odot}\mathrm{h}^{-1}$, gas particles have $m_{\mathrm{gas}} \approx 2.6 \times 10^{9} M_{\odot}\mathrm{h}^{-1}$ depending on their enrichment history, and stellar particles have $m_{\mathrm{stellar}} \approx 7.5 \times 10^{8} M_{\odot}\mathrm{h}^{-1}$ depending on the state of the underlying stellar population. The simulation includes various physical processes: thermal conduction, star-formation and chemical enrichment, growth of BHs and AGN feedback.

1.1 Halo catalogues

Dark matter haloes are defined as gravitationally bound regions in which matter dynamics has decoupled from the Hubble expansion and then collapsed. They are usually characterised by the mass contained within a spherical volume of radius R_{Δ},

$$M_{\Delta} \equiv \frac{4\pi}{3} R_{\Delta}^3 \Delta \rho_c, \tag{2.1}$$

with density proportional to the critical density of the universe $\rho_c = 3H_0^2/8\pi G$ by a factor Δ which defines the (cosmology-dependent) overdensity of a virialised region that undergones spherical collapse; in ΛCDM $\Delta \simeq 180$.

Galaxy clusters are the largest collapsed objects in the Universe. Their distribution in mass and redshift is highly sensitive to cosmological parameters such as the matter density Ω_m, or the amount of matter fluctuations in the Universe σ_8. In the context of hydrodynamical simulations, structures such as clusters or their parent haloes, are defined as locally overdense, self-bound particle groups. Cluster-like haloes catalogues are extracted from the full simulation boxes by identifying these groups of gravitanionally bound particles applying the parallel SUBFIND algorithm (Springel et al. 2001; Dolag et al. 2009).

SUBFIND first step consists in identifying haloes through a Friends-of-Friends (FoF) halo finder. This algorithm relies only on one parameter, b, which defines the linking

[(1)] http://www.magneticum.org

length $L = b \cdot \ell$, proportional to the mean dark matter particle separation, ℓ. The FoF algorithm is run using $b = 0.16$ over the distribution of DM particles only. Since DM particles and baryonic particles are in general distributed differently, it would be problematic to apply the FoF algorithm to all particles at once on an equal footing: this would not lead to selection of groups that are bounded by a clearly defined density contour (that would be the same DM overdensity contour) independently of the presence or absence of baryons, and producing systematic biases in the relative mass content of baryons and DM. The catalogue of gravitationally bound objects that in general contain a mixture of DM, star and gas particles is obtained using the following procedure: each gas and star particle is then associated with its nearest DM particle, i.e., if this DM particle belongs to a FoF group, then the corresponding baryonic particle is also associated with the same group. This effectively encloses all baryonic material as part of a FoF group that is contained in the original DM overdensity contour.

The centre of each halo is identified with the minimum of the gravitational potential occurring among the member particles of the FoF group. Since for observational reasons real masses are measured in terms of spherical overdensity (SO) masses, following the spherical top-hat collapse model, the position of this minimum is taken as the centre balls whose radius is increased until the mean density attains the required overdensity Δ_c. The mass $M_{\Delta c}$ within this spherical region of radius $R_{\Delta c}$ is given by equation (2.1).

Using this procedure (Springel et al. 2001; Dolag et al. 2009) one obtains of cluster-like halo mock catalogues for all the redshift snapshots of the comoving volume $Box2$, with masses $7 \times 10^{12}\, h^{-1} M_\odot < M_{500c} < 2 \times 10^{15}\, h^{-1} M_\odot$, equivalent to $10^{13}\, h^{-1} M_\odot < M_{200m} < 3 \times 10^{15}\, h^{-1} M_\odot$, where M_{200m} is the mass defined with respect to an overdensity of 200 times the universe mean density ρ_m.

1.2 Halo mass function and properties

The comoving number density of haloes of mass M is given by the halo mass function (HMF) defined in equation (1.67), where the variance of the matter density field smoothed with a top-hat window function $W(r)$ of radius $R = (3M/4\pi\overline{\rho}_m)^{1/3}$, i.e. $W(r) = \Theta(r)\Theta(R - r)$ in terms of the Heaviside function Θ, is

$$\sigma^2(M, z) \equiv \frac{1}{2\pi^2} \int P(k, z) \hat{W}^2(kR) k^2 \mathrm{d}k \,, \tag{2.2}$$

where $P(k, z)$ is the linear matter spectrum at redshift z and $\hat{W}$ is the Fourier transform of $W(r)$. The HMF multiplicity function $\phi(\sigma)$ is often parametrised as

$$\phi(\sigma) = A \left[\left(\frac{\sigma}{b} \right)^{-a} + 1 \right] \mathrm{e}^{-\frac{c}{\sigma^2}} \,, \tag{2.3}$$

where the parameters A, a, b, and c need to be calibrated on simulations or data. The HMF fitting function is universal for a linking length $b = 0.2$, or, in a more practical way for observations, for a suitable SO Δ_{mean}, e.g. the universal mass definition can be expressed in terms of Δ_{200m} (Tinker et al. 2008).

Departures from universality are allowed by parametrising a possible redshift dependence of the HMF in Δ_{200m} as a power law in $1+z$:

$$\begin{aligned} A(z) &= A_0(1+z)^{A_z} \\ a(z) &= a_0(1+z)^{a_z} \\ b(z) &= b_0(1+z)^{b_z} \\ c(z) &= c_0(1+z)^{c_z}\,, \end{aligned} \tag{2.4}$$

where the subscript 0 denotes the values at redshift $z = 0$, and where A_z, a_z, b_z, c_z are additional phenomenological parameters. A comprehensive summary of these parameters presented in Figure 2.2, while he result of the HMF fitting for Magneticum simulations is shown in Figure 2.1. Note that one can calibrate the HMF for other definitions of halo masses, such as Δ_{500c}, which is a convenient mass definition within X-ray studies of clusters where the emission is concentrated within the core where n_e is highier, hence cannot easily be traced beyond R_{500c}, or Δ_{200c}, used for measurements of cluster galaxy velocity dispersion and for weak gravitational lensing shear profiles.

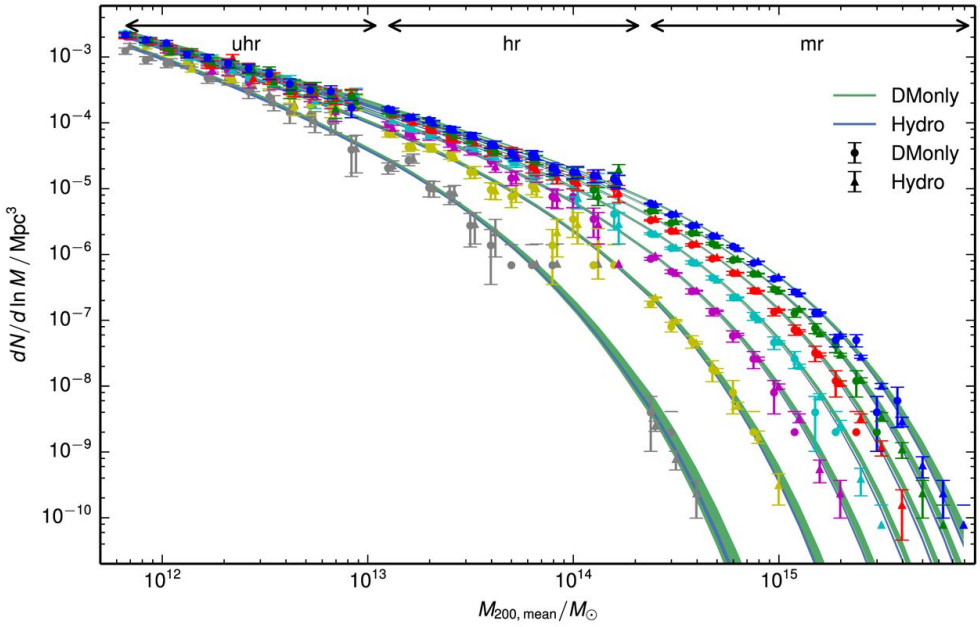

Figure 2.1: HMF $\mathrm{d}N/\mathrm{d}\ln M$ from Magneticum hydro and DMonly simulations. Redshift is increasing from top to bottom and takes values $z = 0,\ 0.13,\ 0.3,\ 0.5,\ 0.8,\ 1.2,\ 2$. The data points are slightly offset in mass for improved readability. The 2σ allowed regions of Hydro (blue region) and DMonly (green region) fits are also shown (Bocquet et al. 2016).

Making the assumption that the HMF is approximately universal in Δ_{200_m}, the HMF

for Δ_{500c} is obtained by a simple change of variables,

$$\frac{\mathrm{d}n}{\mathrm{d}M_{500c}} = \frac{\mathrm{d}n}{\mathrm{d}M_{200m}} \frac{\mathrm{d}M_{200m}}{\mathrm{d}M_{500c}} = \left(-\phi(\sigma) \frac{\overline{\rho}_m}{M^2} \frac{\mathrm{d}\ln\sigma}{\mathrm{d}\ln M_{500c}} \right) \frac{M_{500c}}{M_{200m}} \,. \tag{2.5}$$

The last factor accounts for the conversion between the two different SO mass definitions, which is possible assuming a cluster density profile and a mass-concentration relation. Using the parametrisations by Navarro, Frenk & White (1997) and Duffy et al. (2008) the analytic fit for M_{500c}/M_{200_m} depends on mass, redshift, and Ω_m

$$\frac{M_{500c}}{M_{200m}} \equiv \alpha + \beta \ln \frac{M_{500c}}{M_\odot} \,. \tag{2.6}$$

This prescription reproduces the mass conversion at the few per cent level in the range $0 < z < 2$, $10^{13} < M_{500c}/M_\odot < 10^{16}$, and $0.1 < \Omega_m < 0.5$. The parameters α and β are functions of Ω_m and redshift, and well-approximated by

$$\begin{aligned} \beta(\Omega_m) &= -1.70 \times 10^{-2} + \Omega_m 3.74 \times 10^{-3} \\ \alpha(\Omega_m, z) &= \alpha_0 \, \frac{\alpha_1 z + \alpha_2}{z + \alpha_2} \\ \alpha_0(\Omega_m) &= 0.880 + 0.329\Omega_m \\ \alpha_1(\Omega_m) &= 1.00 + 4.31 \times 10^{-2}/\Omega_m \\ \alpha_1(\Omega_m) &= -0.365 + 0.254/\Omega_m \,. \end{aligned} \tag{2.7}$$

This conversion can be used in an analogous way to establish the form of the HMF for Δ_{200c}.

Parameter	A	a	b	c	A_z	a_z	b_z	c_z
M_{200m}								
DMonly	0.175	1.53	2.55	1.19	−0.012	−0.040	−0.194	−0.021
Hydro	0.228	2.15	1.69	1.30	0.285	−0.058	−0.366	−0.045
M_{200c}								
DMonly	0.222	1.71	2.24	1.46	0.269	0.321	−0.621	−0.153
Hydro	0.202	2.21	2.00	1.57	1.147	0.375	−1.074	−0.196
M_{500c}								
DMonly	0.241	2.18	2.35	2.02	0.370	0.251	−0.698	−0.310
Hydro	0.180	2.29	2.44	1.97	1.088	0.150	−1.008	−0.322

Figure 2.2: Best-fitting HMF parameters for DMonly and hydro simulations (Bocquet et al. 2016).

Among the various halo properties listed in the catalogues, we are interested in the z-component of the velocities, which is aligned along the line-of-sight. One expects a distribution decreasing in absolute value with increasing halo mass, as shown indeed in Figure 2.3.

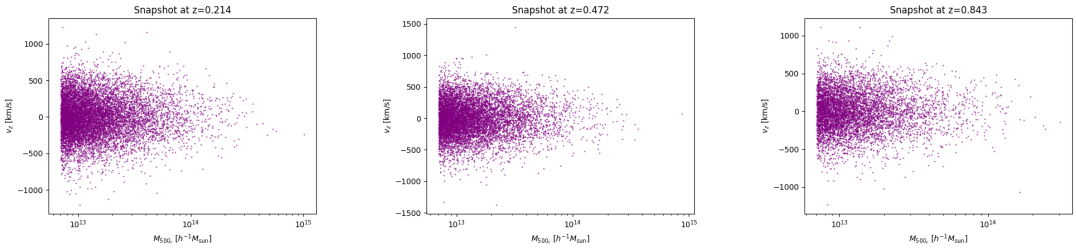

Figure 2.3: Correlations between the v_z component and M_{500c} at three different reshifts (left-to-right: $z = 0.214$, $z = 0.472$, $z = 0.843$).

1.3 kSZ lightcone map

The Magneticum simulations allowed the creation of kSZ signal maps (Dolag et al. 2005). Ideally these maps would be created by placing an observer at one corner of the simulation box and solving the lightcone equation for every gas particle, interpolating their positions between snapshots (Flender et al. 2016). Only gas particles within the lightcone would then contribute to the kSZ map. This approach is, however, not feasible for hydrodynamical simulations, as the gas properties cannot be interpolated safely between snapshots (one would miss shocks, for example). Not relying on the snapshots, on the other hand, would add significantly to the computational complexity of the simulation.

It is therefore convenient to approximate the full lightcone by a series of independent redshift slices making use of the `SMAC` code (Dolag et al. 2005). The kSZ map used for this work is based on the lightcone from the Box2/hr simulation produced for the eROSITA (Predehl et al. 2014) cluster working group and consists of 27 slices between $z \simeq 0.017$ and $z \simeq 2.154$ with Δz increasing from ~ 0.0332 to ~ 0.3120 with redshift (see Table 2.1). For each slice it is necessary to consider a region of appropriate width and depth from the simulation box at the corresponding redshift $z_{\rm tab}$. The kSZ signal is then obtained from the slices via equation (1.46) by projecting along the z-axis of the simulation box. The maps for the full lightcone are then simply given by the co-addition of the signals from the individual slices. The map size is then determined by the size of the simulation box and the highest desired redshift. For $z_{\rm max} \simeq 2$, this yields a map size of $\simeq 5$ deg, corresponding to an area of $\simeq 25$ deg^2. This angular scale is compatible with the flat sky approximation.

The five lowest redshift bins ($z < 0.214$) are not taken into consideration because their volumes only marginally contribute to the lightcone, therefore including very few clusters. Similarly, redshift bins above $z = 0.843$ would provide a poor statistics as clusters start to become rare structures (see Figure 2.1). Since the kSZ signal appears at the location of clusters, it is then necessary to evaluate the angular coordinate of haloes in the lightcone geometry. For this purpose one first extract the cutouts corresponding to the lightcone from the whole simulation box, by using the provided lightcone geometry.

Redshift slice	$z_{\rm tab}$	Δz	depth [Mpc]	width [Mpc]	Redshift slice	$z_{\rm tab}$	Δz	depth [Mpc]	width [Mpc]
$0.017 < z < 0.050$	0.034	0.033	139	13	$0.595 < z < 0.647$	0.621	0.052	161	200
$0.050 < z < 0.085$	0.067	0.034	142	25	$0.647 < z < 0.700$	0.673	0.054	162	214
$0.085 < z < 0.120$	0.102	0.035	144	37	$0.700 < z < 0.756$	0.728	0.055	162	228
$0.120 < z < 0.157$	0.138	0.037	146	50	$0.756 < z < 0.813$	0.784	0.057	162	242
$0.157 < z < 0.194$	0.175	0.038	149	63	$0.813 < z < 0.872$	0.843	0.059	162	256
$0.194 < z < 0.233$	0.214	0.039	151	76	$0.872 < z < 0.934$	0.903	0.061	161	270
$0.233 < z < 0.274$	0.253	0.040	152	89	$0.934 < z < 1.005$	0.965	0.071	181	285
$0.274 < z < 0.315$	0.294	0.042	154	103	$1.005 < z < 1.112$	1.045	0.107	259	305
$0.315 < z < 0.358$	0.336	0.043	156	116	$1.112 < z < 1.252$	1.181	0.140	316	330
$0.358 < z < 0.402$	0.380	0.044	157	130	$1.252 < z < 1.401$	1.326	0.149	312	357
$0.402 < z < 0.448$	0.425	0.046	158	144	$1.401 < z < 1.591$	1.480	0.190	363	387
$0.448 < z < 0.496$	0.472	0.047	159	158	$1.591 < z < 1.842$	1.709	0.250	429	422
$0.496 < z < 0.544$	0.520	0.049	160	172	$1.842 < z < 2.154$	1.983	0.312	469	461
$0.544 < z < 0.595$	0.569	0.050	161	186					

Table 2.1: Redshift slices used for the creation of the lightcone.

Then one converts the objects positions from comoving Cartesian to angular coordinates (or image pixels). In this way, 4363 haloes are selected from the 14 redshift snapshots in the redshift range $0.214 < z < 0.843$.

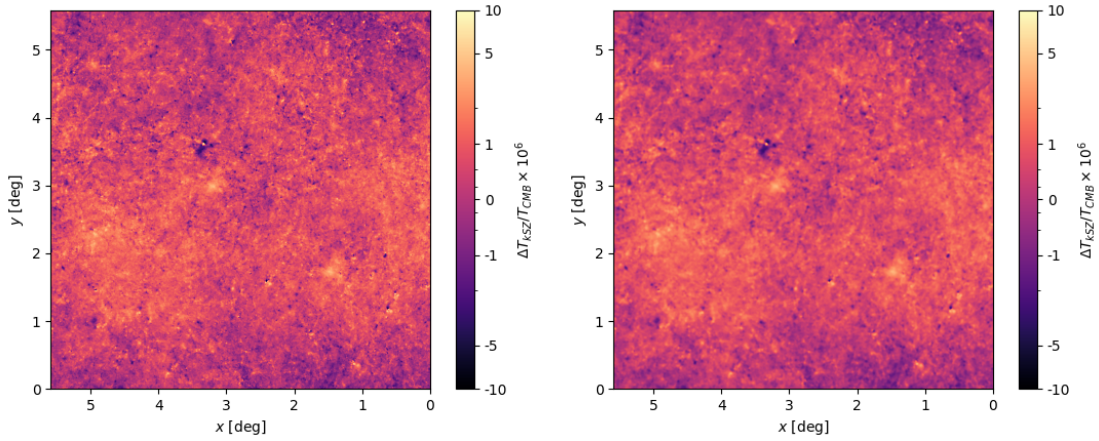

Figure 2.4: kSZ maps: raw unconvolved map (*left panel*), and map convolved with a Gaussian beam with FWHM of $1.2'$ (*right panel*).

2 kSZ signal by aperture photometry

The physically relevant quantity is the optical depth integrated (averaged) within an angular aperture $\theta_{\rm A}$. In this study, this is directly measured from the simulated kSZ map. In order to recreate real (beam-convolved) CMB data, the kSZ map has been convolved with a Gaussian beam with FWHM of $1.2'$, which is representative of

high-resolution CMB surveys operated for example by ACT and SPT.

The kSZ signal is then extracted for each cluster at position $\hat{\mathbf{r}}_0$ by convolution

$$\Delta T(\hat{\mathbf{r}}_0) = \int \mathrm{d}^2\hat{\mathbf{r}}\, T(\hat{\mathbf{r}}) W(|\hat{\mathbf{r}} - \hat{\mathbf{r}}_0|)\,, \tag{2.8}$$

where $W(|\hat{\mathbf{r}} - \hat{\mathbf{r}}_0|)$ is the filter or window function with support fitting the cluster extension. For simulated kSZ maps one can use the trivial filter

$$W_{\mathrm{avg}}(\theta) = \frac{1}{\pi\theta_{\mathrm{A}}^2} \times \begin{cases} 1 & \text{if } \theta < \theta_{\mathrm{A}} \\ 0 & \text{if } \theta > \theta_{\mathrm{A}} \end{cases}, \tag{2.9}$$

which defines an average over pixels within the aperture θ_{A} centred on the cluster position. This is not appropriate for real CMB maps, where the kSZ signal on scales $\theta > \theta_{\mathrm{A}}$ can be masked by the dominant CMB primary anisotropies or other secondary temperature anisotropies, especially due to the tSZ effect and CMB-lensing (Dodelson 2003). For this purpose, a routinely used window function, the aperture photometry (AP) filter, which consists in a compensated filter: the average temperature is computed in pixels within a disk of aperture θ_{A} centred on each cluster and corrected by subtraction of the average temperature of the pixels in each adjacent annulus with external radius $\sqrt{2}\theta_{\mathrm{A}}$ and thus equal area, corresponding to the sky background. That is,

$$W_{\mathrm{AP}}(\theta) = \frac{1}{\pi\theta_{\mathrm{A}}^2} \times \begin{cases} 1 & \text{if } \theta < \theta_{\mathrm{A}} \\ -1 & \text{if } \theta_{\mathrm{A}} < \theta < \sqrt{2}\theta_{\mathrm{A}} \\ 0 & \text{if } \theta > \sqrt{2}\theta_{\mathrm{A}} \end{cases}, \tag{2.10}$$

such that $\int W_{\mathrm{AP}}(\theta)\mathrm{d}^2\boldsymbol{\theta} = 2\pi \int W_{\mathrm{AP}}(\theta)\,\theta\mathrm{d}\theta$. The choice of θ_{A} deserves specific attention. Although a fixed aperture makes the analysis simpler, the haloes virial size in the sample varies by several arcminutes, from $\theta_{\mathrm{vir}} \simeq 1'$ for haloes with $M_{\mathrm{vir}} \simeq 9 \times 10^{12}\, h^{-1} M_\odot$ ($M_{500c} \simeq 7 \times 10^{12}\, h^{-1} M_\odot$) at $z = 0.843$ to $\theta_{\mathrm{vir}} \simeq 9'$ for $M_{\mathrm{vir}} \simeq 3 \times 10^{14}\, h^{-1} M_\odot$ ($M_{500c} \simeq 2 \times 10^{14}\, h^{-1} M_\odot$) at $z = 0.214$. A fixed angular aperture therefore probes different fractions of the cluster for a high-mass/low-z object than for a low-mass/high-z one; the signal associated with the target cluster decreases considering pixels outwards from the centre, by choosing a smaller aperture size that focuses on the brightest inner region, one would maximise the signal-to-noise measurement in real CMB maps. The pitfall of the ring subtraction in this case is that it does not only remove extraneous signals but also part of the genuine kSZ signals. For these reasons, since the Magneticum mock catalogue lists for every object (halo) the projected virial radii $\theta_{\mathrm{vir}} = R_{\mathrm{vir}}/d_A$ (where d_A is the angular diameter distance at the redshift of the object) one can use an adaptive aperture for the analysis. This choice largely, but not entirely, avoids the risk of eliminating part of the genuine signal from the outskirts when apllying the AP filter. Furthermore with $\theta_{\mathrm{A}} = \theta_{\mathrm{vir}}$ one minimises the scatter in the $\Delta T_{\mathrm{kSZ}} - v_{\mathrm{halo}}$ relation.

Chapter 3

Modellisation of peculiar velocities

Many approaches exist to estimate the peculiar velocity field of point-like biased sources like galaxies or clusters of galaxies. In the nearby universe, radial velocities can be inferred from measurements of distances and redshifts obtained from spectroscopy (see Appendix A). For objects further than ~ 200 Mpc measurements are impeded by errors that linearly increase with distance, so one can only estimate velocities using some indirect method. Several reconstruction techniques exist (perturbative, based on Eulerian or Lagrangian schemes; non-perturbative, e.g. based on the least action principle or on optimal transport theory; probabilistic; etc.), all requiring the knowledge of the underlying density field. The following sections present two of them, including the preliminary steps needed to estimate the velocity of galaxy clusters and finally model the kSZ signal.

1 Linear model: Eulerian perturbation theory

In the gravitational instability scenario, the velocity of collisionless test particles is determined by the underlying mass density field.

Starting from the standard equations for an ideal fluid, so the continuity equation and Euler's equation, and relating them to the peculiar velocity field $\mathbf{v}$, one gets the continuity equation for a fluid in comoving coordinates

$$\dot{\delta} + \frac{1}{a}\nabla \cdot (1+\delta)\mathbf{v} = 0\,. \tag{3.1}$$

If it is assumed that the matter is only slightly perturbed from the background cosmological model $\rho(\mathbf{x},t) = \rho_b(t) + \delta(\mathbf{x},t)$ with $\delta \ll 1$, the continuity equation can be be reduced to its linear approximation

$$\dot{\delta} + \frac{1}{a}\nabla \cdot \mathbf{v} = 0\,, \tag{3.2}$$

moreover the overdensity field δ is generally a function of both position and time, while in linear perturbation theory a separation of variables can be performed, handing

$$\delta(\mathbf{x}, t) = D(t)\delta(\mathbf{x})\,, \tag{3.3}$$

where $D(t)$ is the linear growth factor. Substituting for δ thus factorised in (3.2) one gets

$$\nabla \cdot \mathbf{v} = -aHf\delta\,, \tag{3.4}$$

that is the linearised continuity equation in real-space expressed in proper coordinates, where f is the logarithmic growth factor $f = \mathrm{d}\ln D/\mathrm{d}\ln a$. Instead of describing the variables evolution with redshift, integrating between snapshots along the line-of-sight, the mock lightcone is constructed by simply stacking the various snapshots of the Universe, each taken at a given redshift, providing a real-space depiction. This is justified by the fact that the overdensity field δ can be considered to be only position-dependent.

The solution the continuity equation (3.4) can be obtained by means of three-dimensional Fourier transform

$$\hat{\delta}(\mathbf{k}) \equiv \ \mathscr{F}[\delta(\mathbf{x})] \ = \int_{\mathbb{R}^3} \delta(\mathbf{x}) e^{-i2\pi\mathbf{x}\cdot\mathbf{k}}\,, \tag{3.5}$$

handing

$$\mathbf{v}_p = aHf\mathscr{F}^{-1}\left[\frac{i\mathbf{k}}{k^2}\,\hat{\delta}\right]\,. \tag{3.6}$$

To go further, one has to associate the total density field to that of tracers, such as clusters of galaxies, δ_{cl}. Assuming a deterministic linear bias model, $\delta_{\mathrm{cl}} = b\delta$, equation (3.4) becomes

$$\nabla \cdot \mathbf{v} = -aHf\frac{\delta_{\mathrm{cl}}}{b}\,. \tag{3.7}$$

The solution for $\mathbf{v}$ therefore needs the preliminary estimation of the cluster (halo) bias.

2 Halo bias

Collapsed structures such as galaxies, galaxy groups or galaxy clusters are biased tracers of the underlying mass distribution. This is a result of the small-scale physical processes affecting structure formation, which determine the different spatial distribution of baryons and dark matter. The current comprehension of galaxy formation is still partial, and bias schemes or functions are a way to parametrise this ignorance in statistical spatial analysis. According to the spherical collapse model, structures do not form in sites randomly sprinkled around space, but at specific locations where the local overdensity exceeds a given threshold and then collapse, cooling and star formation can occur. It is plausible that baryons condense more efficiently into collapsed objects in regions where peaks of the density field can be found. This would suggest that non-baryonic matter is not distributed the same way as the visible baryonic matter. This

simple idea, together with the assumption that the cosmological density field is Gaussian on very large scales, led Kaiser (1984) to suggest a biased structure formation scheme.

Since velocities are generated by gravitational instability of all the gravitating matter, they provide a mean to study the total distribution of matter. Indeed, unless doing gravitational lensing measurements, only the baryonic portions of cosmic structures are observed; the relationship between the total and baryonic (cluster) mass defines the bias. The building element for bias estimates is the two-point correlation function $\xi(r)$, which describes the excess probability with respect to a uniform distribution to find two objects at spatial separation r.

The correlation function of objects (clusters) and the matter auto-covariance function are not equivalent: the overall matter distribution is smoother the galaxies or galaxy clusters mass distribution. Suppose the density field δ_M, smoothed on some appropriate mass scale M to define a collapsed object, is a zero-mean, stationary, Gaussian random field. All the statistics specifying its properties are encoded in its auto-covariance function

$$\xi(r) = \langle \delta_M(\mathbf{x}) \delta_M(\mathbf{x}') \rangle \,, \tag{3.8}$$

where the average is taken over all spatial positions $\mathbf{x}$ and $\mathbf{x}'$ such that $|\mathbf{x} - \mathbf{x}'| = r$ (the ergodic hypothesis holds). If for example galaxy clusters were faithful tracers of mass, then their two-point correlation function $\xi_{\rm cc}(r)$ would coincide with $\xi(r)$. In reality this relation is not valid, as galaxy clusters form in special high-density sites where density exceeds some threshold $\delta_{\rm c} = \nu\sigma_{\rm M}$, with ν dimensionless threshold and $\sigma_{\rm M}$ the field variance defined as $\sigma^2_{\rm M} = \xi(0)$. In the simplest, linear bias scheme for clusters, one has $\delta_{\rm cc} = b\delta_M$

The two-point correlation function of these overdense regions (identified with galaxy clusters) and the corresponding quantity for the full density field $\xi(r)$ follow the simplified linear relation

$$\xi_{\rm cc}(r) \simeq b^2 \xi(r) \,, \tag{3.9}$$

with $b = \nu/\sigma_{\rm M}$. The two-point correlation function for the full density field, $\xi(r)$, is obtained by Fourier transfor of the total matter power spectrum computed with CAMB, using the Hankel transformations[(1)]that is an extension of the FastFourier Transform (FFT) for logarithmically spaced sequences. The clusters correlation function is computed from the Magneticum catalogue using the Landy & Szalay (1993) estimator

$$\hat{\xi}_{\rm cc}(r) = \frac{DD(r)f^2 - 2DR(r)f + RR(r)}{RR(r)} \,, \tag{3.10}$$

where f is the ratio of the number of objects in the original catalogue and the number of random points in the random catalogue; $DD(r)$, $DR(r)$ and $RR(r)$ are the object-object, object-random and random-random pair counts, with spatial separation r in the range $[r - \delta r/2, r + \delta r/2]$, where δr is the bin size of the N_b bins in which $\xi_{\rm cc}$ is estimated. In this case $\xi_{\rm cc}(r)$ is computed for the haloes distribution at each of the redshifts available for the Magneticum simulation snapshots in the separation range $6 - 102$ h^{-1}Mpc with

[(1)]https://github.com/minaskar/hankl

linear binning 8 h^{-1}Mpc, with homogeneously distributed random objects 50 times the data. The highly optimized (OPEN-MP parallel) clustering codes CORRFUNC (Sinha & Garrison 2020) have been used for this scope. The peculiarity of CORRFUNC is that it is built following a grid structure instead of a tree structure.[(2)]

Many mocks obtained by bootstrap resampling $\widetilde{\xi_{\rm cc}}$ are used and the error associated to $\xi_{\rm cc}$ is encoded in the associated covariance matrix.

The bias is obtained by χ^2 minimisation, which requires the knowledge of the inverse of the covariance matrix $\mathbf{C}$, namely the precision matrix $\mathbf{\Psi} = \mathbf{C}^{-1}$. Calling $\mathbf{D}$ the data vector $\mathbf{D} = (\xi(r_1), \dots, \xi(r_N))$ and $\mathbf{T}(\theta)$ the model depending on the parameter θ that needs to be estimated, the χ^2 function is given by

$$\chi^2 = \sum_{ij} (D_i - T_i(\theta)) \Psi^{ij} (D_j - T_j(\theta)) \,. \tag{3.11}$$

The covariance matrix $\hat{\mathbf{C}}$ is computed from N independent synthetic datasets $\mathbf{D}^{(k)}$ obtained from the mock catalogue and reproducing realistic data (mimicking SPT/ACT/-Planck cluster catalogues), using the estimator

$$\hat{C}_{ij} = \frac{1}{N_s - 1} \sum_{k=1}^{N_s} (D_i^{(k)} - \bar{D}_i)(D_j^{(k)} - \bar{D}_j) \,, \quad i = 1, \dots, n \,. \tag{3.12}$$

Here $\bar{D} = \frac{1}{N_s} \sum_k D_i^{(k)}$ is the mean value of the measurements at the ith angular bin over the N_s bootstrapped catalogues, which provides an unbiased estimate of the ensemble average $\langle \mathbf{D} \rangle$.

When independent realizations are used, the inverse of $\hat{\mathbf{C}}$ given by equation (3.12) provides a biased estimate of $\mathbf{\Psi}$, this bias can simply be corrected by including a prefactor

[(2)] The volume probed for two-point correlation functions estimates increases as the cubic power of the radius, and the number of particle pairs counted in a bin strongly depends on the outer bound of the radial range specified. For a given outer bound $R_{\rm max}$, to minimize the total number of distance computations, it would be convenient to partition the domain into distinct spatial regions, and then quickly identify pairs of regions where particle pairs cannot be within $R_{\rm max}$. Tree structures map the entire domain into a 'root node', and then recursively sub-divide the domain into 'leaves' when some specified (maximum) threshold of particles is reached at any 'node'. Such an adaptive, hierarchical spatial partitioning requires more complex tree construction algorithms and consequently, tree construction also frequently imposes a significant runtime overhead. In a grid structure, the entire domain is sub-divided into a grid with a fixed spatial width. Such a sub-division necessitates either knowing the entire domain extent a priori (a case satisfied for simulation boxes) or, calculating the spatial extent by making a pass through the entire set of particles. Once the spatial extent is known, the partitions are simple axis-aligned sub-divisions of the specified width. Such a sub-division forms a crucial difference between the grid and the tree partitioning schemes. In the tree case, the number of partitions depends on both the spatial extent and the actual number and distribution of particles, while in the grid case the total number of partitions only depends on the domain extent and is independent of the number and distribution of particle positions. Compared to grids, tree structures often have better theoretical scaling $\sim \mathcal{O}(N \log N)$ or even $\mathcal{O}(N)$. However, modern CPUs so strongly prefer the ordered memory access enabled by grid structures that often grids end up providing the faster time-to-solution. For this reason computations relying on simulation boxes containing a large number of objects are better tackled by using fast codes such as CORRFUNC.

as

$$\mathbf{\Psi} = \left(1 - \frac{N_b + 1}{N_s - 1}\right)\hat{\mathbf{C}}^{-1}\,. \tag{3.13}$$

The off-diagonal elements of $\hat{\mathbf{C}} = [C_{ij}]$ of a general measurement might exhibit a large dispersion, in estimates of the two-point correlation function values of two non-adjacent bins (one very far apart from the other) show a very small covariance. As a consequence $\mathbf{\Psi}$ is ill-conditioned, i.e., the ratio between its smallest and largest eigenvalue is smaller than the machine precision, resulting in uncontrolled inverse $\mathbf{C}^{-1}$. The covariance tapering method (Paz & Sánchez 2015) allows for a down-weighting of the contribution of points with very small covariance (which typically have a low signal-to-noise ratio), avoiding the propagation of errors into the regression and then into final cosmological constraints. This method consists in defining a tapered covariance matrix $\mathbf{C}^t$ from the estimate $\hat{\mathbf{C}}$ of equation (3.12) by means of a so called tapering matrix $\mathbf{T}$ as

$$\mathbf{C}^t = \hat{\mathbf{C}} \circ \mathbf{T}\,, \tag{3.14}$$

where $\circ$ indicates the Hadamard (or elemnt-wise) product. The tapering matrix $\mathbf{T}$ is defined as an isotropic covariance matrix by means of a taper function K

$$T_{ij} = K(\parallel r_i - r_j \parallel)\,, \tag{3.15}$$

where r_i is the ith measurement location on the data space (e.g. the bin separation for correlation function measurements) and K is defined e.g. as

$$K(x) = \begin{cases} \left(1 - \frac{x}{T_p}\right)^4\left(4\frac{x}{T_p} + 1\right) & \text{if } x < T_p \\ 0 & \text{if } x \geq T_p\,. \end{cases} \tag{3.16}$$

The tapering parameter T_p defines the size of the support function of K (in this study $T_p = 60$ Mpc).

When using the tapering method, the estimation of the precision matrix simply as the inverse of the tapered covariance $\mathbf{C}^t$ can introduce systematic biases on the obtained parameter constraints. However, by applying a second Hadamard product to the inverse of $\mathbf{C}^t$ and estimating the precision matrix as

$$\mathbf{\Psi}^t = \left(1 - \frac{N_b + 1}{N_s - 1}\right)\left(\hat{\mathbf{C}} \circ \mathbf{T}\right)^{-1} \circ \mathbf{T} \tag{3.17}$$

it is possible to obtain an unbiased and robust estimate of the precision matrix. Recalling that the realisations are given by ξ_{cc} and the model corresponds to $b^2\xi$ and replacing $\mathbf{\Psi}$ in equation (3.11), by the two-tapered precision matrix estimator, $\mathbf{\Psi}^t$, the minimisation of χ^2 function gives

$$b^2 = \left(\xi^{\mathrm{T}}\,\mathbf{\Psi}^t\,\xi^{\mathrm{T}}\right)^{-1}\xi^{\mathrm{T}}\,\mathbf{\Psi}^t\,\xi_{cc}\,. \tag{3.18}$$

Recalling that for a parameter θ whose best fit value is $\hat{\theta}$

$$\hat{\sigma}^2_\theta = \left(\frac{1}{2}\frac{\partial^2\chi^2}{\partial\theta^2}\right)^{-1}\Bigg|_{\theta=\hat{\theta}} \tag{3.19}$$

the uncertainty on b^2 is given by

$$\sigma_{b^2}^2 = \left(\xi^{\mathrm{T}} \mathbf{\Psi}^t \xi\right)^{-1}. \tag{3.20}$$

The uncertainty on b, σ_b^2, is finally obtained using the standard rules of quadratic error propagation.

z_{tab}	b
0.214	1.99 ± 0.02
0.253	2.07 ± 0.02
0.294	2.10 ± 0.02
0.336	2.16 ± 0.03
0.380	2.21 ± 0.03
0.425	2.25 ± 0.03
0.472	2.34 ± 0.03
0.520	2.36 ± 0.03
0.569	2.42 ± 0.04
0.621	2.50 ± 0.04
0.673	2.60 ± 0.04
0.728	2.65 ± 0.04
0.784	2.73 ± 0.04
0.843	2.87 ± 0.04

Table 3.1: Values of bias and its error for every redshift snapshot

3 Linear model: numerical solution

Once the halo bias is known, one can numerically solve equation (3.7) starting from a continuous sampling of the onerdensity field δ at each redshift snapshot of Magneticum $Box2$/hr simulation.

The first step consists in associationg the particles (haloes) positions on a 256^3 Cartesian grid, using the triangular-shape cloud (TSC) mass-assignment scheme. This has been achieved using the Pylians[(3)]library for the analysis of numerical simulations.

Then the density field is smoothed with a Gaussian filter W_R of radius $R = 4$ Mpc$/h$, which is the typical radius of galaxy clusters, working in Fourier space, i.e., using direct

[(3)]https://pylians3.readthedocs.io/en/master/

$\mathscr{F}$ and inverse $\mathscr{F}^{-1}$ Fourier transformations[4]yielding

$$\delta_R = \mathscr{F}^{-1}\left[\mathscr{F}[\delta]\mathscr{F}[W_R]\right] . \tag{3.21}$$

One can finally obtain the peculiar velocity field interpolated on the original Cartesian grid. Since the kSZ signal depends on the velocity component along the line-of-sight, which in the parallel-plane approximation coincides with the z-direction of the simulation snapshots, it is sufficient to solve for

$$v_z^{\rm rec} = a\frac{Hf}{b}\mathscr{F}^{-1}\left[\frac{ik_z}{k^2}\,\hat{\delta_{cc}}\right] . \tag{3.24}$$

Once the full v_z field is obtained, the line-of-sight component of the velocity for each object is found on the grid pixels that corresponds to the nearest grid point to the objects positions (a more accurate localisation can use bilinear interpolation).

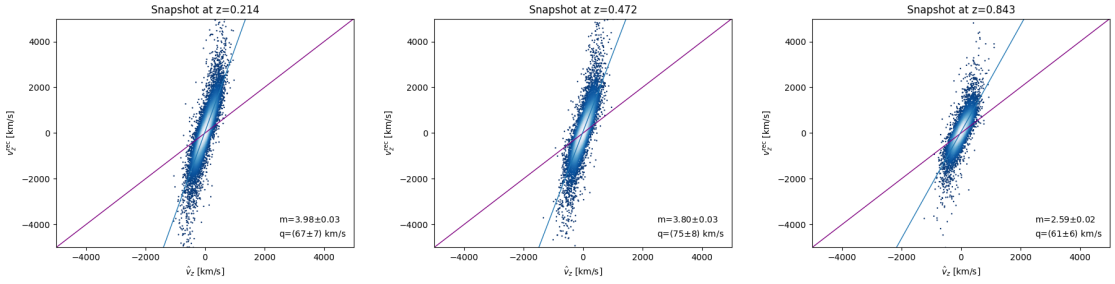

Figure 3.1: Correlations between N-body and reconstructed velocities along the $\hat{z}$ axis, v_z^* and $v_z^{\rm rec}$, at three different reshifts (left panel $z = 0.214$, central panel $z = 0.472$, right panel $z = 0.843$).

This simple reconstruction scheme overestimates the velocities, as shown in the scatter plots in Figure 3.1. A linear regression of reconstructed velocities as function of N-body (true) velocities, $v_z^{\rm rec} - mv_z^{N\rm body} + q$, shows that the former are highly biased,

[4]Given that the density field has been interpolated on a grid, it requires to be handled using discrete Fourier transforms (DFT)

$$\mathscr{F}[\delta(x,y,z)] = \sum_{x=0}^{N-1}\sum_{y=0}^{N-1}\sum_{z=0}^{N-1}\delta(x,y,z)e^{-\frac{i2\pi}{N}(k_{\rm x}x+k_{\rm y}y+k_{\rm z}z)} \tag{3.22}$$

$$\mathscr{F}^{-1}[\hat{\delta}(k_{\rm x},k_{\rm y},k_{\rm z})] = \frac{1}{N}\sum_{k_{\rm x}=0}^{N-1}\sum_{k_{\rm y}=0}^{N-1}\sum_{k_{\rm z}=0}^{N-1}\hat{\delta}(k_{\rm x},k_{\rm y},k_{\rm z})e^{-\frac{i2\pi}{N}(k_{\rm x}x+k_{\rm y}y+k_{\rm z}z)} . \tag{3.23}$$

These operations are computed using the Fast Fourier Transform (FFT), a method for computing the DFT with reduced execution time. To further optimise the computational time it is convenient to use the built-in Python function Scipy FFT[5], which performs better than the concurrent built-in function Numpy FFT.

[5]https://docs.scipy.org/doc/scipy/reference/fft.html#module-scipy.fft

	No σ-clipping		σ-clipping	
z	m	q [km/s]	m	q [km/s]
0.214	3.98 ± 0.03	67 ± 7	3.62 ± 0.02	62 ± 5
0.253	3.89 ± 0.03	68 ± 7	3.54 ± 0.02	63 ± 5
0.294	3.88 ± 0.03	70 ± 7	3.56 ± 0.02	66 ± 5
0.336	3.85 ± 0.03	71 ± 7	3.52 ± 0.02	68 ± 5
0.380	3.90 ± 0.03	74 ± 8	3.47 ± 0.02	71 ± 6
0.425	3.90 ± 0.03	75 ± 8	3.42 ± 0.02	67 ± 6
0.472	3.80 ± 0.03	75 ± 8	3.41 ± 0.02	65 ± 6
0.520	3.83 ± 0.03	85 ± 8	3.45 ± 0.02	76 ± 6
0.569	3.93 ± 0.03	87 ± 8	3.54 ± 0.02	76 ± 6
0.621	4.06 ± 0.03	91 ± 9	3.54 ± 0.02	72 ± 6
0.673	3.97 ± 0.03	85 ± 9	3.51 ± 0.03	78 ± 7
0.728	3.97 ± 0.04	90 ± 9	3.49 ± 0.03	81 ± 7
0.784	3.88 ± 0.04	92 ± 9	3.45 ± 0.03	80 ± 7
0.843	3.73 ± 0.04	89 ± 9	3.36 ± 0.03	80 ± 7

Table 3.2: Linear regression parameters for $(v_z^{\rm rec}, v_z^{\rm Nbody})$ scatter with and without σ-clipping. In the main text $v_z^{\rm Nbody}$ is also indicated with v_z^*

with $m \sim 3.9$, and shifted by $q \sim 80$ km/s, i.e., producing a fictitious bulk flow. Nonetheless, reconstructed and true velocities are very correlated (sample Pearson correlation coefficient $r = 0.79$), allowing for a fairly robust correction of reconstructed velocities that can better estimate the true ones

$$v_z^{\rm rec} \to \hat{v}_z^{\rm rec} = \frac{1}{m}\big(v_z^{\rm rec} - q\big)\,. \tag{3.25}$$

In order to improve the linear regression and obtain a more robust estimation of true velocities, it is possible to remove outliers by performing a σ-clipping. This procedure consists in iterating over the data and rejecting at each step the values that differ in absolute value from a central value more than n standard deviations. Using a configuration of 3σ-clipping and iterating for a maximum of three times, the new linear regression yield a smaller bias, $m \sim 3.5$, a slightly smaller offset, $q \sim 70$ km s^{-1}, and larger correlation coefficient, $r = 0.83$, supporting a more accurate rescaling (results shown in Table 3.2 and Figure 3.2). The new map to estimate the true velocities is then

$$\hat{v}_z^{{\rm rec},\sigma} = 0.2857(v_z^{\rm rec} - 70) \quad \left[{\rm km\,s^{-1}}\right]\,. \tag{3.26}$$

The uncertainty on the velocity estimates is given by the residual of the rescaled velocities, $\hat{v}_z^{{\rm rec},\sigma}$, with respect to its expectation value v_z^*.

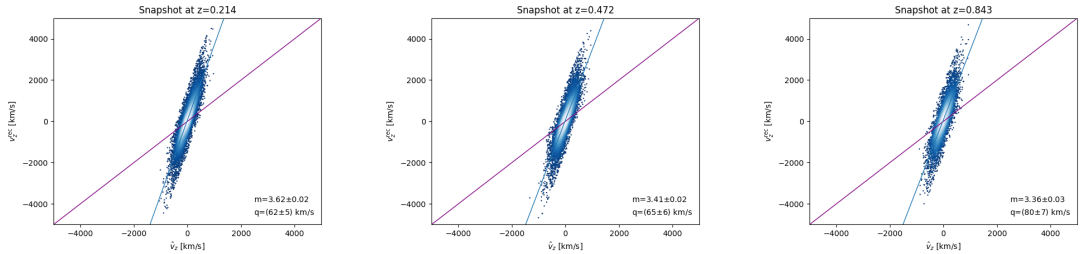

Figure 3.2: Correlations between N-body and reconstructed velocities along the $\hat{z}$ axis, v_z^* and $v_z^{\rm rec}$, at three different reshifts (left panel $z = 0.214$, central panel $z = 0.472$, right panel $z = 0.843$) after σ-clipping. Compared to the analysis without σ-clipping shown in Figure 3.1, the correlation coefficient is larger consistently with smaller dispersion; σ-clipping provides a better estimator for true velocities.

4 Non linear model: eFAM

At low redshift and on small scales cosmic structures evolve following a non-linear regime, i.e. attaining large values of local overdensity that prevent any perturbative approach. Consistently linear reconstruction techniques are not appropriate anymore.

Fully non-linear techniques, in which simplifying assumptions are not made on the dynamical state of the system but rather of the orbits of the objects, can overcome these problems. Outstanding fully non-linear methods for relating the present peculiar velocity and density fields are based on the least action principle (LAP; Peebles 1989). The equations of motion of tracers can be derived from the stationary variations of the action with respect to trajectories subject to fixed mixed boundary conditions, namely final (observed) positions and vanishing initial peculiar velocities of clusters in this case.

A first efficient version of fully non-linear methods based on the cosmological least action principle (LAP; Peebles 1989; Branchini & Carlberg 1994), which yield the full trajectory of tracers along with their velocities as a byproduct, is the Fast Action Minimization (FAM) algorithm (Nusser & Branchini 2000; Romano et al. 2005), which has been developed to recover the past orbits of point-like particles both in real-and redshift-space in an Einstein-De Sitter Universe. An extension to the original algorithm dubbed eFAM (Sarpa et al. 2019) is extended to a generic cosmology and is able to reconstruct the orbits of more than $N = 10^5$ objects with computational complexity to $O(N)$, thus allowing its application to larger datasets with respect to FAM.

The eFAM algorithm consists in minimizing the action of the system of N point-like tracers with known bias

$$S = \int_0^{t_0} \mathrm{d}t \left[\sum \frac{m_i a^2}{2} \left(\frac{\mathrm{d}x_i}{\mathrm{d}t} \right)^2 + \frac{G}{a} \sum_{i \neq j} \frac{m_i m_j}{|\mathbf{x}_i - \mathbf{x}_j|} + \frac{2}{3} \pi G \rho_b a^2 \sum m_i \mathbf{x}_i^2 \right] \tag{3.27}$$

with respect to the unknown coefficients $C_{i,n}$, which parameterise the orbits of each

particle as $\mathbf{x}_i(D)$=$\mathbf{x}_{i,\rm obs} + \sum_{n=0}^{M} C_{i,n} q_n(D)$, i.e., a linear combination of M polynomials $q_i(D)$ function of the growth factor D and suitably chosen to guarantee the mixed boundary conditions mentioned above. Once the orbits are known, the velocity of each object is obtained as $\mathbf{v}_i$=$(\mathrm{d}\mathbf{x}_i/\mathrm{d}D)(\mathrm{dD}/\mathrm{d}t)$.

Remark: Because of limitation of computational resources, the modelling of the kSZ signal by eFAM velocities was not possible. It is left for a future study.

5 Non linear model: phenomenological approach

Regarding the non-linear techniques it may be interesting to quantify the extent to which a deviation of the reconstructed peculiar field can take place from its real value and determine a non-negligible impact on the estimate of the optical depth. This analysis can be achieved by constructing a perturbed peculiar velocity field drawing a value for the velocity from a multivariate Gaussian probability density function,

$$\mathbf{v} \sim \mathcal{N}\big(\boldsymbol{\mu}, \mathbf{C}\big) = \frac{1}{(2\pi)^{3/2}\sqrt{\det\,\mathbf{C}}}\,\exp\left[-\frac{1}{2}(\mathbf{v}-\boldsymbol{\mu})^{\mathrm{T}}\mathbf{C}^{-1}(\mathbf{v}-\boldsymbol{\mu})\right], \tag{3.28}$$

with $\boldsymbol{\mu} = \mathbf{M}\mathbf{v} + \mathbf{q}$ and $\mathbf{M} = \mathrm{diag}(m_x, m_y, m_z)$ diagonal matrix with elements depending on the bias parameter (see later). Supposing uncorrelated velocities, i.e., a diagonal covariance matrix $\mathbf{C}$, the velocity along one axis, for instance $\hat{z}$, is a one-dimensional Gaussian variate,

$$v_z \sim \mathcal{N}\big(\mu_z, \sigma_z\big) = \frac{1}{\sqrt{2\pi}\sigma_z}\,\exp\left[-\frac{(v_z-\mu_z)^2}{2\sigma_z^2}\right], \tag{3.29}$$

with mean

$$\mu_z^i = m^i v_z^* + q^i\,, \tag{3.30}$$

given by the real line-of-sight velocity value perturbed with a multiplicative bias m_i and an offset q_i, with index $i = 1, \ldots, 11$ denoting a fixed value of bias b (see Table 4.1). The velocity dispersion σ_z is taken from previous reconstructions of velocities considering Magneticum *Box*2 (Sarpa et al. 2019).

By obtaining a model on how the estimate of the average optical depth $\overline{\tau}$ of clusters gets degraded with respect to how biased of far from the true velocities is a reconstruction, it is possible to set accuracy limits on reconstruction techniques. The accuracy of a velocity reconstruction technique has to fall inside these limits in order to give a reasonable estimate on $\overline{\tau}$.

Chapter 4

Results and prospects

The goal of this study was to compare the kSZ signal extracted from the synthetic map from the Magneticum (hydrodynamical) simulations to the model based on reconstructed values of clusters velocity along the line-of-sight, v_z, giving an estimate of the optical depth τ. The kSZ signal, i.e. temperature variations ΔT w.r.t. the CMB cosmological signal around the position of galaxy clusters due to their bulk motion is proportional to v_z according to $\Delta T = -\tau v_z/c$: the optical depth is then obtained by linear regression. The temperature signal is extracted from the simulated map, since a substamp of the simulated map can be realised with arbitrary large precision by finer resampling, $\Delta T_{\rm AP}$ and $\Delta T_{\rm avg}$ are considered without error. Reconstructed velocities v_z are instead uncertain, as described in Chapter 3 (Section 3), their precision and accuracy depending on the specific technique, on the estimation of the bias of clusters and on the spatial resolution of the underlying matter field. A linear regression is therefore computed for $v_z(\Delta T_{\rm AP})$ and $v_z(\Delta T_{\rm avg})$; Figure 4.1 shows instead the inverse relations $\Delta T_{\rm AP}(v_z)$ and $\Delta T_{\rm avg}(v_z)$ to facilitate the interpretation of the slope as proportional to τ.

The correlation method applied to the Magneticum kSZ map combined with linear perturbation theory reconstruction of velocities (equation (3.24)) yield the following results:

- the correlation method gives $\tau_{\rm avg} = (2.5253 \pm 0.0008) \times 10^{-3}$ and $\tau_{\rm AP} = (1.2890 \pm 0.0008) \times 10^{-3}$, obtained without cleaning the data with a σ-clipping procedure,
- $\tau_{\rm avg} = (2.6625 \pm 0.0001) \times 10^{-4}$ and $\tau_{\rm AP} = (9.3203 \pm 0.0004) \times 10^{-5}$ after σ-clipping the linear regression.

The errors on τ are very likely underestimated, for further analysis the uncertainty on the optical depth is expected and will be assumed to be more realistically of order of 1%. This first result is presented in Figure 4.1 for σ-clipped data.

The theoretical values of v_z, directly provided by the simulation, are used to obtain fiducial values of τ for both `avg` and AP extraction, which are respectively $\hat{\tau}_{\rm avg} = 3.45 \times 10^{-5}$ and $\hat{\tau}_{\rm AP} = 1.66 \times 10^{-5}$. These fiducial estimates are used to study how

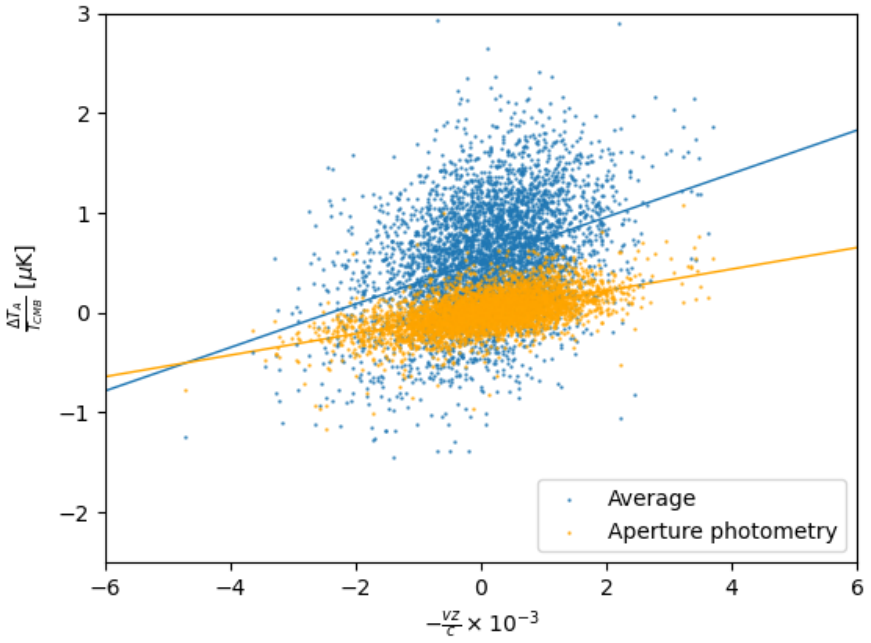

Figure 4.1: Scatter-plot with linear regression of temperature AP values and average disk values with respect to corrected reconstructed velocities.

much the actual value of τ is degraded when the true values of the velocities are not properly recovered by reconstruction. For this purpose Monte Carlo simulations with further 2σ-clipping have been performed to improve the robustness of linear regression. Analysing the results for a non-biased ($m = 1$) Monte Carlo realisation, one can see that the offset does not play a significant role in the estimation of τ, even for values as large as $q = \pm 10000$ km s^{-1}. One needs therefore to investigate the impact of the multiplicative bias m between reconstructed and N-body (true) line-of-sight velocities, $v_z^{\rm rec} \simeq m v_z^{\rm Nbody}$.

The quality of the estimates obtained by varying m are presented in Table 4.1, quoting

$$\Delta\tau_{\rm A} = 100\frac{\tau_{\rm A} - \hat{\tau}_{\rm A}}{\hat{\tau}_{\rm A}} \tag{4.1}$$

as the relative residual of $\tau_{\rm A}$ with respect to the fiducial values for several values of m.

From the results shown in Figure 4.1 it becomes very apparent that the optical depth estimates obtained with the AP filter are biased low with respect to the ones obtained with just the simple average-filter without background subtraction. This difference arises because clusters are not perfect circles in projection (as if they were fully relaxed and intrinsically spherical) and also do not have a sharp edge at $\theta_{\rm vir}$. The average optical

m	$\tau_{\rm avg}/10^{-5}$	$\Delta\tau_{\rm avg}$	$\tau_{\rm AP}/10^{-5}$	$\Delta\tau_{\rm AP}$
0.5	7.02	104	3.30	99
0.6	5.88	70	2.75	65
0.7	4.82	40	2.33	41
0.8	4.34	26	2.09	26
0.9	3.81	11	1.84	11
1.1	3.13	9	1.51	9
1.2	2.80	19	1.35	19
1.4	2.48	28	1.20	28
1.6	2.17	37	1.03	38
1.8	1.95	43	0.93	44
2.0	1.72	50	0.83	50

Table 4.1: Optical depth derived by N-body ("true") velocities perturbed by a multiplicative factor m (first column; see equation (3.30)) and computed from the kSZ maps as average within disks ($\tau_{\rm avg}$, second column) or by aperture photometry ($\tau_{\rm AP}$, fourth column). The absolute deviations from the true values computed using the N-body velocities are indicated as percent values (respectively, third and fifth column). The impact of a possible offset of reconstructed velocities (dubbed q in equation (3.30)) is negligible.

depth of a cluster within an aperture $\theta_{\rm A}$, dubbed $\langle\tau\rangle_{\rm A}$, and its *cylindrical* gas mass are related through

$$M^{\rm cyl}_{\rm gas,A} = \int_{\rm cyl} {\rm d}V \rho_{\rm gas} = \frac{d_{\rm A}^2 \mu_e m_p}{\sigma_{\rm T}} \int_{\theta_{\rm A}} {\rm d}\Omega \int {\rm d}l n_e \sigma_{\rm T} = \frac{\mu_e m_p}{\sigma_{\rm T}} \, \pi \, \theta_{\rm A}^2 d_{\rm A}^2 \langle\tau\rangle_{\rm A} \, , \qquad (4.2)$$

where $\mu_e \simeq 1.14$ is the mean particle weight per electron (assuming primordial abundances) and m_p is the proton mass. The AP estimate subtracts contributions from $\theta_{\rm vir} < \theta < \sqrt{2}\theta_{\rm vir}$ from the signal within $\theta_{\rm vir}$, thus reducing the measured $M^{\rm cyl}_{\rm gas,A}$ and therefore τ. If one were to compare an estimate of $M^{\rm cyl}_{\rm gas,A}$ to the true value obtained directly from the simulation particle data, one would find that *i)* $M^{\rm cyl}_{\rm gas,avg}$ obtained by averaging on the aperture disk is indeed a better estimator of the true value; *ii)* $M^{\rm cyl}_{\rm gas,AP}$ would be biased, with bias increasing with decreasing apertures ($\theta_{\rm A} \lesssim \theta_{500}$), thus it should decrease when including more particles from the cluster outskirts ($\theta_{\rm A} \gtrsim \theta_{\rm vir}$) (Soergel et al. 2018). The average-filtered $\tau_{\rm avg}$ is therefore a better estimator of the true integrated cylindrical gas mass when dealing with simulated signals. The larger

dispersion of $\tau_{\rm avg}$ values with respect to $\tau_{\rm AP}$ ones is likely due to spurious signal from other nearby clusters that is not fully removed by background subtraction.

The pairwise estimator would have the advantage of averaging to zero any signal associated with individual clusters, i.e. the tSZ effect. However, the decision to instead adopt the *velocity correlation method* for kSZ detections, has been prompted by the fact that the scale at which the pairwise kSZ signal starts to disappear is around $r_{\rm max} \approx$ 300 Mpc: the use of this estimator for a simulation box of size 352 Mpc h^{-1} would lead to a biased low estimate of the signal, being this bias exacerbated when restricting to a lightcone FoV of 25 deg^2 with maximum comoving width of 256 Mpc. If bigger volumes were provided, the use of this estimator would be appropriate, nonetheless it has to be handled with care. When constructing the kSZ map the way in which the simulation box gets sliced may not preserve large-scale correlations between adjacent slices. If the typical comoving thickness of a redshift slice only differs by a factor $2-3$ from $r_{\rm max}$, the pairwise kSZ signal at the largest scales would be biased low because by construction we have removed the correlation between cluster pairs from different slices. For this reason, when considering the pairwise signal, galaxy clusters gatalogues should be divided in redshift bins that coincide with the redshift limits of the kSZ lightcone slices.

One could also asses how much the convolution with a Gaussian beam of FWHM $= 1.2'$ affects the estimate of τ. The convolution broadens the signal therefore part of it falls in the outside ring and gets subtracted when AP is performed, leading to an underestimation of τ. Comparing the two fiducial values (using the real velocities) with and without convolution, dubbed $\tau_{\rm AP}^{beam}$ and $\tau_{\rm AP}^{no-beam}$, one obtains $\tau_{\rm AP}^{beam}/\tau_{\rm AP}^{no-beam} \approx 0.77$, consistently with the estimates obtained by Soergel et. al (2018).

A natural step further in the development of this study would be using reconstructed velocities given by the eFAM algorithm, which is expected to perform within the window of a few percent of τ degradation (especially true for reconstructions obtainde considering redshift space corrections). This study will require adequate computational resources.

Then it would be interesting to test other simulations, such as SIMBA (Davé et al. 2019) or Illustris-TNG (Nelson et al. 2019), and to test the pairwise estimator provided that a large FoV is available.

The final, perhaps more interesting application would be testing this method for the determination of the optical depth τ on data such as BOSS (Anderson et al. 2012)[(1)], eBOSS (Dawson et al. 2016)[(2)], DESI (DESI Collaboration 2023)[(3)], or 4MOST/Galaxy Clusters Survey (Finoguenov et al.)[(4)] jointly analysed with ACTPol (Naess et al. 2014) or SPT (Andersson et al. 2011) following e.g. Schaan et al. (2016). Eventually one can perform analysis using the Euclid clusters extracted from the spectroscopic catalogue covering a redshift range $0.9 < z < 1.8$ (Euclid Collaboration 2020)[(5)] combined with Simons Observatory data (The Simons Observatory Collaboration 2019).

[(1)] https://www.sdss3.org/surveys/boss.php
[(2)] https://www.sdss4.org/surveys/eboss/
[(3)] https://www.desi.lbl.gov/
[(4)] https://www.4most.eu/cms/home/
[(5)] https://euclid.caltech.edu/

Appendix A

Measurements of distances and redshifts

In a Robertson-Walker metric, distance is given by $r = a\chi$, where $a(t)$ is the scale factor at time t, denoted a_0 at the present day, $\chi(\overline{z})$ is the comoving distance of an object at cosmological redshift $\overline{z}$[1]

$$\chi(\overline{z}) = \frac{c}{a_0}\int_0^{\overline{z}} \frac{\mathrm{d}z}{H(z)}\,. \tag{A.1}$$

Then the total velocity of an object is obtained by differentiation of distances with respect to time $v = \dot{a}\chi + a\dot{\chi}$, so it becomes apparent that velocities are partly due to the Hubble expansion $\overline{v} = \dot{a}\chi = Hr$, where $H(t) = \dot{a}(t)/a(t)$, and partly due to peculiar motion $v_p = a\dot{\chi}$

$$v = \overline{v} + v_p\,. \tag{A.2}$$

Historically peculiar velocities have been often inferred from independent measurements of distances and redshifts, this allows to separate the peculiar term v_p from the recession term $\overline{v}$, a technique whose failings are highlighted in Davis & Scrimgeour (2014). When an object has a peculiar velocity, it acquires an additional redshift component z_p to the cosmological redshift due to Hubble flow $\overline{z}$. The relationship between the peculiar velocity component on the line of sight and z_p is

$$v_p = cz_p\,, \tag{A.3}$$

in the non-relativistic case, or

$$v_p = c\frac{(1+z_p)^2 - 1}{(1+z_p)^2 + 1}\,, \tag{A.4}$$

in the relativistic case. An object with $\overline{z}$ and z_p will appear to an observer to have z given by

$$(1+z) = (1+\overline{z})(1+z_p)\,. \tag{A.5}$$

[1] Overbars denote quantities that would be measured in a perfectly homogeneous and isotropic universe without peculiar velocities.

The first naïve approximation to estimate v_p from distances and redshifts would be

$$v_p = cz - H_0 r\,, \tag{A.6}$$

so the radial peculiar velocity v_p is the difference between cz, with z is the observed redshift, and $\overline{v} = H_0 r$, with r proper distance discussed previously. The relation (A.6) is based on the approximation $v = cz$, which is assumed since calculating total velocity from observed redshift is tricky (as it needs knowledge of the peculiar velocity which is what is being sought after), and fails at high redshifts. Moreover the relationship between redshift and recession velocity does not follow $\overline{v} = c\overline{z}$, so it is best to carry peculiar velocity estimations by working in redshifts, never translating them to velocities. If $v_p = cz - H_0 r$ is estimated by calculating r for each recession redshift $\overline{z}$ using equation (A.1) and $r = a\chi$, and the redshift one would observe z if the object had a peculiar velocity v_p, obtained using equations (A.3) or (A.4) and (A.5), it becomes clear that this approximation is a poor one as it would overestimate v_p by about 100 km/s even as close as $z = 0.04$ [80]. This can be fixed by working in redshifts as previously suggested and use the measured r to infer what the recession redshift, $\overline{z}$, obtain z_p by rearranging (A.5)

$$z_p^{\text{correct}} = \frac{z - \overline{z}}{1 + \overline{z}}\,, \tag{A.7}$$

and then substitute z_p^{correct} into the equation for peculiar velocity (A.3) or (A.4)

$$v_p^{\text{correct}} = c\frac{z - \overline{z}}{1 + \overline{z}}\,. \tag{A.8}$$

Using this method the dependence of the estimation of v_p on the cosmological model lays in the inference of $\overline{z}$ from r.

Bibliography

[1] Sunyaev R. A., Zel'dovich Ya. B., *The observation of relic radiation as a test of the nature of X-ray radiation from the clusters of galaxies*, 1972, Comments Astrophys. Space Phys., 4, 173.

[2] Zel'dovich Ya. B., Sunyaev R. A., *The interaction of matter and radiation in a hot-model universe*, 1969, Ap&SS, 4, 301-316.

[3] Sunyaev R. A., Zel'dovich Ya. B., *Small-scale fluctuations of relic radiation*, 1970, Ap&SS, 7, 1.

[4] Sunyaev R. A., Zel'dovich Ya. B., *The velocity of clusters of galaxies relative to the microwave background. The possibility of its measurement*, 1980, MNRAS, 190, 413-420.

[5] Birkinshaw M., *The Sunyaev-Zel'dovich effect*, 1999, PhR, 310, 97-195.

[6] Carlstrom J. E., Holder G.P., Reese E. D., *Cosmology with the Sunyaev-Zel'dovich effect*, 1999, ARA&A, 40, 643-680.

[7] Rephaeli Y., *Comptonization Of The Cosmic Microwave Background: The Sunyaev-Zeldovich Effect*, 1995, ARA&A, 33, 541-580.

[8] Mroczkowski T., Nagai D., Basu K. et al., *Astrophysics with the Spatially and Spectrally Resolved Sunyaev-Zeldovich Effects. A Millimetre/Submillimetre Probe of the Warm and Hot Universe*, 2019, SSRv, 215, 17.

[9] Fixsen D. J., *The Temperature of the Cosmic Microwave Background*, 2009, ApJ, 707, 916-920.

[10] Kompaneets A. S., *The Establishment of Thermal Equilibrium between Quanta and Electrons*, 1956, ZhETF, 31, 876.

[11] Bernstein J., Dodelson S., *Aspects of the Zel'dovich-Sunyaev mechanism*, 1990, PhRvD, 41, 354-373.

[12] Phillips P. R., *Calculation of the Kinetic Sunyaev-Zeldovich Effect from the Boltzmann Equation*, 1995, ApJ, 455, 419.

[13] Battistelli E. S., *Experimental Astrophysics*, IOP Publishing, 2021.

[14] Serra G., Sirmain C., Lamarre J. M. et al., *The PRONAOS telescope* 1998, in Proc. ICSO Conf., Toulouse, Poster Session 2.

[15] Parijskij Y. N., *Detection of Hot Gas in the Coma Cluster of Galaxies*, 1972, AZh, 49, 1322.

[16] Gull S. F., Northover K. J. E., *Detection of hot gas in clusters of galaxies by observation of the microwave background radiation*, 1976, Nature, 263, 572.

[17] Lake G., Partridge R. B., *Detection of intergalactic gas in distant, rich clusters*, 1977, Nature, 270, 502.

[18] Birkinshaw M., Gull S. F., Northover K. J. E., *Extent of hot intergalactic gas in the cluster Abell 2218*, 1978, Nature, 275, 40-41.

[19] Holzapfel W. L., Wilbanks T. M., Ade P. A. R. et al., *The Sunyaev-Zeldovich Infrared Experiment: A Millimeter-Wave Receiver for Cluster Cosmology*, 1997, ApJ, 479, 17-30.

[20] Benoît A., Zagury F., Coron N. et al., *Calibration and rst light of the Diabolo photometer at the Millimetre and Infrared Testa Grigia Observatory* 2000, A&AS, 141, 523-532.

[21] Lamarre J.M., Giard M., Pointecouteau E. et al., *First Measurement of the Submillimeter Sunyaev-Zel'dovich Effect*, 1998, ApJ Letters, 507, L5-L8.

[22] Niemack M. D., Zhao Y., Wollack, E. et al., *A Kilopixel Array of TES Bolometers for ACT: Development, Testing, and First Light*, 2008, JLTP, 151, 690-696.

[23] Staniszewski Z., Ade P. A. R., Aird K. A. et al., *Galaxy Clusters Discovered with a Sunyaev-Zel'dovich Effect Survey*, 2009, ApJ, 701, 32-41.

[24] Menanteau F., González, J., Juin J.-B. et al., *The Atacama Cosmology Telescope: Physical Properties and Purity of a Galaxy Cluster Sample Selected via the Sunyaev-Zel'dovich Effect*, 2010, ApJ, 723, 1523-1541.

[25] Bersanelli M., Mandolesi N., Butler R.C. et al., *Planck pre-launch status: Design and description of the Low Frequency Instrument*, 2010, A&A, 520, A4.

[26] Lamarre J.-M., Puget J.-L., Ade P. A. R. et al., *Planck pre-launch status: The HFI instrument, from specification to actual performance*, 2010, A&A, 520, A4.

[27] Planck Collaboration, *The Scientific Programme of Planck (Bluebook)* 2005, ESA publication ESA-SCI(2005)/01.

[28] Mroczkowski T., Dicker S., Sayers J. et al., *A Multi-wavelength Study of the Sunyaev-Zel'dovich Effect in the Triple-merger Cluster MACS J0717.5+3745 with MUSTANG and Bolocam*, 2012, ApJ, 761, 47.

[29] Sayers J., Mroczkowski T., Zemcov M. et al., *A Measurement of the Kinetic Sunyaev-Zel'dovich Signal Toward MACS J0717.5+3745*, 2013, ApJ, 778, 52.

[30] Dicker S. R., Korngut P. M., Mason B. S. et al., *MUSTANG: 90 GHz science with the Green Bank Telescope*, 2008, Proc. SPIE, 7020, 702005.

[31] Haig D. J., Ade P. A. R., Aguirre J. E. et al., *Bolocam: status and observations*, 2004, Proc. SPIE, 5498, 78-94.

[32] Monfardini A., Benoît A., Bideaud A. et al., *A Dual-band Millimeter-wave Kinetic Inductance Camera for the IRAM 30 m Telescope*, 2011 ApJ, 194, 24.

[33] Adam R., Bartalucci I., Pratt G. W. et al., *Mapping the kinetic Sunyaev-Zel'dovich effect toward MACS J0717.5+3745 with NIKA*, 2017, A&A, 598, A115.

[34] Jones M., Saunders R., Alexander P. et al., *An image of the Sunyaev-Zel'dovich effect*, 1993, Nature, 365, 320-323.

[35] Birkinshaw M., Hughes J. P., *A Measurement of the Hubble Constant from the X-Ray Properties and the Sunyaev-Zel'dovich Effect of Abell 2218*, 1994, ApJ, 420, 33.

[36] Dawson K. S., Holzapfel W. L., Carlstrom J. E. et al., *A Preliminary Detection of Arcminute-Scale Cosmic Microwave Background Anisotropy with the BIMA Array*, 2001, ApJL, 553, L1-L4.

[37] Ueda S., Kitayama T., Oguri M. et al., *A Cool Core Disturbed: Observational Evidence for the Coexistence of Subsonic Sloshing Gas and Stripped Shock-heated Gas around the Core of RX J1347.5-1145*, 2018, ApJ, 866, 48.

[38] Ferreira P. G., Juszkiewicz R., Feldman H. A. et al., *Streaming Velocities as a Dynamical Estimator of* Ω, 1999. ApJ, 515, L1–L4.

[39] Hand N., Addison G. E., Aubourg E., et al., *Evidence of Galaxy Cluster Motions with the Kinematic Sunyaev-Zel'dovich Effect*, 2012, Phys. Rev. Letters, 109, 041101.

[40] Planck Collaboration, *Planck intermediate results. XXXVII. Evidence of unbound gas from the kinetic Sunyaev-Zeldovich effect*, 2015, A&A, 586, A140.

[41] Schaan E. et al. (ACTPol Collaboration), *Evidence for the kinematic Sunyaev-Zel'dovich effect with ACTPol and velocity reconstruction from BOSS*, 2016, Phys. Rev. D, 93, 8.

[42] Cavaliere A., Danese L., De Zotti G., *Unborn clusters*, 1977, ApJ, 217, 6.

[43] Cavaliere A., Danese L., De Zotti G., *Cosmic distances from X-ray and microwave observations of clusters of galaxies*, 1979, A&A, 75, 322.

[44] Silk J., White S. D. M., *The determination of* q_0 *using X-ray and microwave observation of galaxy clusters*, 1978, ApJL, 226, L103.

[45] Cavaliere A., Fusco-Femiano R., *X-rays from hot plasma in clusters of galaxies*, 1976, A$A, 49, 137-144.

[46] Cavaliere A., Fusco-Femiano R., *The Distribution of Hot Gas in Clusters of Galaxies*, 1978, A$A, 70, 677.

[47] Mattig W., *Über den Zusammenhang zwischen Rotverschiebung und scheinbarer Helligkeit*, 1958, Astronomische Nachrichten, 284, 109.

[48] Reese E. D., Mohr J. J., Carlstrom J. E. et al., *Sunyaev-Zeldovich Effect-derived Distances to the High-Redshift Clusters MS 0451.6-0305 and CL 0016+16*, ApJ, 533, 38.

[49] Reese E. D., Carlstrom J. E., Joy M. K. et al., *Determining the Cosmic Distance Scale from Interferometric Measurements of the Sunyaev-Zeldovich Effect*, 2002, ApJ, 581, 53.

[50] Planck collaboration, *Planck 2013 results. XX. Cosmology from Sunyaev–Zeldovich cluster counts*, 2014, A&A, 571, A20.

[51] Planck collaboration, *Planck 2015 results. XXIV. Cosmology from Sunyaev-Zeldovich cluster counts*, 2016, A&A, 594, A24.

[52] Komatsu E., Seljak U., *The Sunyaev-Zel'dovich angular power spectrum as a probe of cosmological parameters*, 2002, MNRAS, 336, 1256.

[53] Planck collaboration, *Planck intermediate results. III. The relation between galaxy cluster mass and Sunyaev-Zeldovich signal*, 2013, A&A, 550, A129.

[54] Press W. H., Schechter P., *Formation of Galaxies and Clusters of Galaxies by Self-Similar Gravitational Condensation*, 1974, ApJ, 187, 425-438.

[55] Sheth R. K., Tormen G., *Large-scale bias and the peak background split*, 1999, MNRAS, 308, 119-126.

[56] Tinker J., Kravtsov A. V., Klypin A. et al., *Toward a Halo Mass Function for Precision Cosmology: The Limits of Universality*, 2008, ApJ, 688, 709.

[57] Watson W. A., Iliev I. T., D'Aloisio A. et al., *The halo mass function through the cosmic ages*, 2013, MNRAS, 433, 1230-1245.

[58] Grego L., Carlstrom J. E., Reese E. D. et al., *Galaxy Cluster Gas Mass Fractions from Sunyaev-Zeldovich Effect Measurements: Constraints on* $\Sigma_{\rm m}$, 2001, ApJ, 552, 2-14.

[59] Peebles P. J. E., *The Large-Scale Structure of the Universe*, Princeton Univ. Press, 1980.

[60] Suszkiewicz R., Springel V., Durrer R., *Dynamics of Pairwise Motions*, 1999, ApJ, 518, L25-L28.

[61] Planck collaboration, *Planck intermediate results. XLVII. Planck constraints on reionization history*, 2016, A&A, 596, A108.

[62] Zahn O., Reichardt C. L., Shaw L. et al., *Cosmic Microwave Background Constraints on the Duration and Timing of Reionization from the South Pole Telescope*, 2012, ApJ, 756, 65.

[63] Shaw L. D., Rudd D. H., Nagai D., *Deconstructing the Kinetic SZ Power Spectrum* , 2012, ApJ, 756, 15.

[64] Smith K. M. and Ferraro S., *Detecting Patchy Reionization in the Cosmic Microwave Background*, 2017, PhRvL, 119, 021301.

[65] Battaglia N., Natarajan A., Trac H. et al., *Reionization on Large Scales. III. Predictions for Low-l Cosmic Microwave Background Polarization and High-l Kinetic Sunyaev-Zel'dovich Observables*, 2013, ApJ, 776, 83.

[66] Kamionkowski M., Loeb A., *Getting around cosmic variance*, 1997, PhRvD, 56, 8.

[67] S. Y. Sazonov, Sunyaev R. A., *Microwave polarization in the direction of galaxy clusters induced by the CMB quadrupole anisotropy*, 1999, MNRAS, 310, 3, 765-772.

[68] Wechsler R. H., Tinker J. L., *The Connection Between Galaxies and Their Dark Matter Halos*, 2018, ARA&A, 56, 435-487.

[69] Somerville R. S., Davé R., *Physical Models of Galaxy Formation in a Cosmological Framework*, 2015, ARA&A, 53, 51–113.

[70] Springel V., *The cosmological simulation code GADGET-2*, 2005, MNRAS, 364, 1105-1134.

[71] Komatsu E., Smith K. M., Dunkley J. et al., *Seven-year Wilkinson Microwave Anisotropy Probe (WMAP) Observations: Cosmological Interpretation*, 2011, 192, 18.

[72] Navarro J. F., Frenk C. S., White S. D. M., *A Universal Density Profile from Hierarchical Clustering*, 1997, ApJ, 490, 493-508.

[73] Duffy A. R., Schaye J., Kay S. T. et al., *Dark matter halo concentrations in the Wilkinson Microwave Anisotropy Probe year 5 cosmology*, 2008, MNRAS, 390, L64-L68.

[74] Hirschmann M., Dolag K., Saro A. et al., *Cosmological simulations of black hole growth: AGN luminosities and downsizing*, 2014, MNRAS, 442, 2304–2324.

[75] Bocquet S., Saro A., Dolag K, *Halo mass function: baryon impact, fitting formulae, and implications for cluster cosmology*, 2016, MNRAS, 456, 2361–2373.

[76] Merloni A., Predehl P., Becker W. et al., *eROSITA Science Book: Mapping the Structure of the Energetic Universe*, ArXiv e-prints, [arXiv:1209.3114].

[77] Predehl P., Andritschke R., Becker W. et al., *eROSITA on SRG*, 2014, Proceedings of the SPIE, 9144, 91441T.

[78] Flender S., Bleem L., Finkel H. et al., *Simulations of the Pairwise Kinematic Sunyaev-Zel'dovich Signal* 2016, ApJ, 823, 98.

[79] Dodelson S., *Modern Cosmology* , Academic Press, 2003.

[80] Davis T. M., Scrimgeour M. I., *Deriving accurate peculiar velocities (even at high redshift)*, 2014, MNRAS, 442, 1117-1122.

[81] Phelps S. D., Desjacques V., Nusser A., Shaya E. J., *Numerical action reconstruction of the dynamical history of dark matter haloes in N-body simulations*, 2006, MNRAS, 370, 3.

[82] Dekel A., Reese M. J., *Physical mechanisms for biased galaxy formation*, 1987, Nature, 326, 455-462.

[83] Tinker J. L., Robertson B. E., Kravtsov A. V. et al., *The Large-scale Bias of Dark Matter Halos: Numerical Calibration and Model Tests*, 2010, ApJ, 724, 878–886.

[84] Kaiser N. , *On the spatial correlations of Abell clusters.*, 1984, ApJ, 284, L9-L12.

[85] Landy S. D., Szalay A. S., *Bias and Variance of Angular Correlation Functions*, 1993, ApJ, 412, 64.

[86] Sinha M., Garrison L. H., *CORRFUNC - a suite of blazing fast correlation functions on the CPU*, 2020, MNRAS, 491, 3022-3041.

[87] Paz D. J., Sánchez A. G., *Improving the precision matrix for precision cosmology*, 2015, MNRAS, 454, 4326–4334.

[88] Padmanabhan N., Xu X., Eisenstein D. J. et al., *A 2 per cent distance to z = 0.35 by reconstructing baryon acoustic oscillations - I. Methods and application to the Sloan Digital Sky Survey*, 2012, MNRAS, 427, 2132–2145.

[89] Sarpa E., Schimd C., Branchini E., Matarrese S., *BAO reconstruction: a swift numerical action method for massive spectroscopic surveys*, 2019, MNRAS, 484, 3.

[90] Branchini E., Carlberg R. G., *Testing the Least Action Principle in an Omega 0=1 Universe* 1994, ApJ, 434, 37.

[91] Nusser A., Branchini E., *On the least action principle in cosmology*, 2000, MNRAS, 313, 587.

[92] Romano-Díaz E., Branchini E., van de Weygaert R., *Local supercluster dynamics: external tidal impact of the PSCz sample traced by optimized numerical least action method*, 2005, A&A, 440, 425.

[93] Davé R., Anglés-Alcázar D., Narayanan D., *SIMBA: Cosmological simulations with black hole growth and feedback*, 2019, MNRAS, 486, 2827-2849.

[94] Nelson D., Springel V., Pillepich A. et al., *The IllustrisTNG simulations: public data release*, 2019, Computational Astrophysics and Cosmology, 6, 2.

[95] Anderson L., Aubourg E., Bailey S. et al., *The clustering of galaxies in the SDSS-III Baryon Oscillation Spectroscopic Survey: Baryon Acoustic Oscillations in the Data Release 9 Spectroscopic Galaxy Sample*, 2012, MNRAS, 427, 3435-3467.

[96] Dawson K. S., Kneib J., Percival W. J. et al., *The SDSS-IV Extended Baryon Oscillation Spectroscopic Survey: Overview and Early Data*, 2016, ApJ, 151, 44.

[97] DESI Collaboration, *The Early Data Release of the Dark Energy Spectroscopic Instrument*, 2023, arXiv:2306.06308

[98] Finoguenov A., Merloni A., Comparat J., *4MOST Consortium Survey 5: eROSITA Galaxy Cluster Redshift Survey*, 2019, The Messenger, 175, 39–41.

[99] Naess S., Hasselfield M., McMahon J. et al., *The Atacama Cosmology Telescope: CMB polarization at 200 < ℓ < 9000*, 2014, JCAP, 10, 007.

[100] Andersson K., Benson B. A., Ade P. A. R. et al., *X-Ray Properties of the First Sunyaev-Zel'dovich Effect Selected Galaxy Cluster Sample from the South Pole Telescope* 2011, ApJ, 738, 48.

[101] Euclid Collaboration, *Euclid preparation. X. The Euclid photometric-redshift challenge*, 2020, A&A, 644, A31.

[102] The Simons Observatory Collaboration, *The Simons Observatory: science goals and forecasts*, 2019, JCAP, 02, 056.